Astron. Astrophys. 326, 1117–1134 (1997)

ASTRONOMY AND ASTROPHYSICS

A spectroscopic investigation of P Cygni

I. H and He I lines

F. Najarro[1], **D.J. Hillier**[2], **and O. Stahl**[3]

[1] Institut für Astronomie und Astrophysik der Universität München, Scheinerstr. 1, D-81679 München, Germany
[2] Department of Physics and Astronomy, University of Pittsburgh, 3941 O'Hara Street, Pittsburgh, PA 15260, USA
[3] Landessternwarte Königstuhl, D-69117 Heidelberg, Germany

Received 27 March 1997 / Accepted 3 June 1997

Abstract. We present a detailed spectroscopic analysis of the H and He I spectrum of the Luminous Blue Variable (LBV) P Cygni. The observational constraints for our investigation are given by the mean optical and near-IR spectra obtained by Stahl et al. (1993) and published UV, optical, IR and radio continuum measurements of the star.

Within the parameter domain of interest we have investigated how line strengths, line shapes and the emergent energy distribution behave as a function of stellar parameters such as temperature, luminosity, wind density, etc. The sensitivity of the H and He I line profiles to model parameters allows a quantitative spectroscopic analysis of P Cygni to be performed. The derived parameters for P Cygni place it near a regime where two classes of models exist – those in which H remains fully ionized in the wind, and those in which H eventually recombines in the wind. The transition between the two classes of models is dramatic – a 5% change in luminosity or mass-loss is sufficient. The shape of the P Cygni absorption on the Hα profile and the radio variability indicates that H must recombine in P Cygni's wind.

As for Wolf-Rayet (W-R) stars we find that we can generate a set of homologous models which are capable of explaining, within observational errors, the flux distribution and the line profiles equally well. Scaling relations for the homologous models have been determined, but to first order they have the same $T_{\rm eff}$ and the same wind density parameter ($\dot{M}/R_*^{1.5}$). Consequently it is impossible to derive R_* from a spectroscopic analysis.

Assuming R_*=75 $R_\odot$, the following stellar parameters for P Cygni are derived:

L_*=5.6×10^5 $L_\odot$ ($T_{\rm eff}$=1.82 kK)
n_{He}/n_H=0.3 $\dot{M}$=3.0×10^{-5} $M_\odot$ yr^{-1}
V_∞= 185 km s^{-1} β = 2.5
log $g_{\rm eff}$=1.20.

These imply a stellar distance of 1.7 ± 0.1 kpc, which is consistent with determinations in the literature.

Continuum fluxes and the observed optical and near-infrared H and He I line profiles are well reproduced by the model. The derived stellar parameters and the high helium abundance indicates that P Cygni is highly evolved.

Key words: stars: early-type – stars: mass-loss – stars: atmospheres – stars: supergiants – stars: individual: P Cygni

Send offprint requests to: F. Najarro

1. Introduction

P Cygni is one of the most luminous stars of the Galaxy. It has been classified as an LBV after two major outbursts in 1600 and 1660 which were followed by three decades of irregular photometric variations. After 1700 no major eruption has occurred, although since then the star has been gradually increasing its visual brightness at a rate of $\approx -.15 \pm .02$mag per century (6% decrease in effective temperature every hundred years; Lamers & de Groot 1992). Superimposed on this long-term gradual increase, short-term irregular variations are observed ($\Delta M_v \leq 0.2$, much lower than those of up to 2 magnitudes for other LBVs) which characterize the present variability of the star (Lamers 1986, de Groot 1989). Such variations are thought to be caused by subphotospheric instabilities where the driving mechanism may be related to the presence of the huge iron opacity bump at T$\sim 2\times10^5$K (Stothers & Chin 1994) or to resonances of acoustic modes that generate violent instabilities (Glatzel & Kiriakidis 1993). However, none of the proposed mechanisms provides a self-consistent description of the observations.

Insight into the nature and the evolutionary phase of P Cygni has recently been achieved. On the basis of up-to-date evolutionary and stellar atmosphere models, Langer et al. (1994) showed that the star is at the end of the hydrogen shell burning phase and is evolving to the right of the H-R diagram. This confirms the results of Lamers & de Groot (1992) based on the photometric history of P Cygni in the last three centuries.

Several analyses, of varying degrees of sophistication, have been performed on the emission line spectrum of P Cygni. These studies (e.g., Kuan & Huhi 1975, van Blerkom 1978, Barlow & Cohen 1977, Drew 1985) have given conflicting results, particularly regarding the velocity law and the mass-loss rate of P Cygni. The resolution of these discrepancies is important if we are to understand the mass-loss process in P Cygni, if we are to determine reliable abundances, and if we are to fully understand the evolution of massive stars. With better observational data, and more sophisticated radiative transfer codes, we are in excellent position to resolve some of the outstanding issues regarding P Cygni and its wind.

In this paper we concentrate primarily on average properties of the star and perform a detailed spectroscopic investigation of the mean He and H spectrum of P Cygni. In Sect. 2 we briefly describe the method and assumptions, and list the basic parameters with which we initiated our investigations. The ionization structure of P Cygni's wind, essential for understanding the spectrum of P Cygni, is discussed in Sect. 3. We investigate how line profiles and the emergent energy distribution behave as a function of L_*, $\dot{M}$, and the velocity law within the parameter domain of interest in Sect. 4. The cause of the variations is discussed. In Sect. 5 we investigate homologous models, whose parameters are related by simple scaling laws, which are capable of matching the observed spectrum of P Cygni equally well. This investigation reveals that the radius of P Cygni (and hence its distance) cannot be derived via spectroscopic analysis. Once the dependence of line profiles and continuum on stellar parameters is well understood, we can proceed to model the star in detail. This is done in Sect. 6 where we present and discuss the successes and shortcomings of our current best model for P Cygni. We also present a comparison between our derived velocity law and that determined from a hydrodynamical treatment of the wind of P Cygni. The evolutionary consequences of our model for P Cygni are discussed.

2. Method and model assumptions

We have used the iterative non-LTE method presented by Hillier (1987, 1990) which solves the radiative transfer equation in spherical geometry, subject to the constraints of statistical and radiative equilibrium, for the expanding atmospheres of early-type stars. Polarization observations by Taylor et al. (1991) suggest that while variable asymmetric structures exist in the wind, there is no preferred axis of symmetry suggesting that to first order spherical geometry may be a suitable approximation.

The Sobolev approximation (corrected for the diffuse radiation field) yields a satisfactory description of the extended, dense atmosphere within the parameter domain of interest and therefore has been used for most of the investigation. Several models were computed using the comoving-frame (CMF) transfer equation, and in general the agreement with the Sobolev results were satisfactory (see Sect. 6). For some models there can be substantial differences, although in such cases the difference can be removed by a relatively small adjustment of the stellar parameters. In the investigation of parameter space we solve for a pure H–He atmosphere with 15 H, 49 He I ($n \leq 10$) and 7 He II levels. For the determination of the final stellar parameters calculations were performed in the CMF. As Drew (1985) has shown that CNO lines are important coolants in the wind of P Cygni, and since Johnson et al. (1992) find that the N abundance see in the nebulae surrounding P Cygni is enhanced, we include nitrogen in the final models.

The adopted velocity law

$$v(r) = \frac{V_o + (V_\infty - V_o)\{1 - R_*/r\}^\beta}{1 + (V_o/V_{core})\exp[(R_* - r)/h_{eff}]} \quad (1)$$

is characterized by an isothermal effective scale height in the inner atmosphere, h_{eff}, and becomes a classic β law in the wind. The parameter V_o regulates the transition zone between photosphere and wind, V_∞ is the terminal velocity, and V_{core} is the expansion velocity of the core (i.e., inner boundary). In the present study V_{core} was generally set to $210^{-2}\,km\,s^{-1}$.

Each model is characterized by 7 free parameters. They are R_*, L_*, $\dot{M}$, the He abundance, and the 3 velocity parameters h_{eff}, V_o and β. Since V_∞ can be readily determined from the spectrum it is not treated as a free parameter (although small (e.g., 10%) adjustments are made in determining the best fit value).

As reference values for our investigation we chose stellar parameters close to those derived by Lamers et al. (1983) and confirmed by Pauldrach & Puls (1990). Several slightly different parameters sets have been used in this paper to illustrate important characteristics of the models; the appropriate parameters are listed as each model is discussed.

3. The ionization structure of P Cygni's wind

The stellar parameters for P Cygni place the object in (or very near) a regime where small changes in the stellar parameters (e.g., a change of only 0.05 dex in L_* or $\dot{M}$) can lead to a dramatic switch in the ionization structure of H and He in the wind (see, for example, Pauldrach & Puls 1990). In order to model the stellar spectrum it is crucial to understand which processes determine the run of the wind ionization structure, and what observational constraints can be placed on the ionization structure.

To illustrate the ionization sensitivity we have chosen two model sets for which all stellar parameters are identical except the stellar luminosity (and hence T_{eff}). Common model parameters are as follows:

R_*=75 $R_\odot$	$\dot{M}$=4.4 $\times$ 10^{-5} $M_\odot$ yr^{-1}
V_∞=185 km s^{-1}	β=4
h_{eff}=7.5 $\times$ 10^{-3} R_*	n_{He}/n_H=0.4

For the recombined model we take L_*=8.75$\times 10^5$ $L_\odot$ (T_{eff}=20380K) while for the "ionized" model we adopt L_*=1$\times 10^6$ $L_\odot$ (T_{eff}=21070K).

The H and He ionization structure for both models is shown in Fig. 1a–da. Both H and He are singly ionized throughout the entire wind in the "ionized" model. In the "recombined" model He becomes neutral for $\log \tau_R < -2$ while a switch in the run of the ionization structure of H takes places at $\log \tau_R \approx -1.5$ and neutral hydrogen becomes dominant for $\log \tau_R < -3.5$.

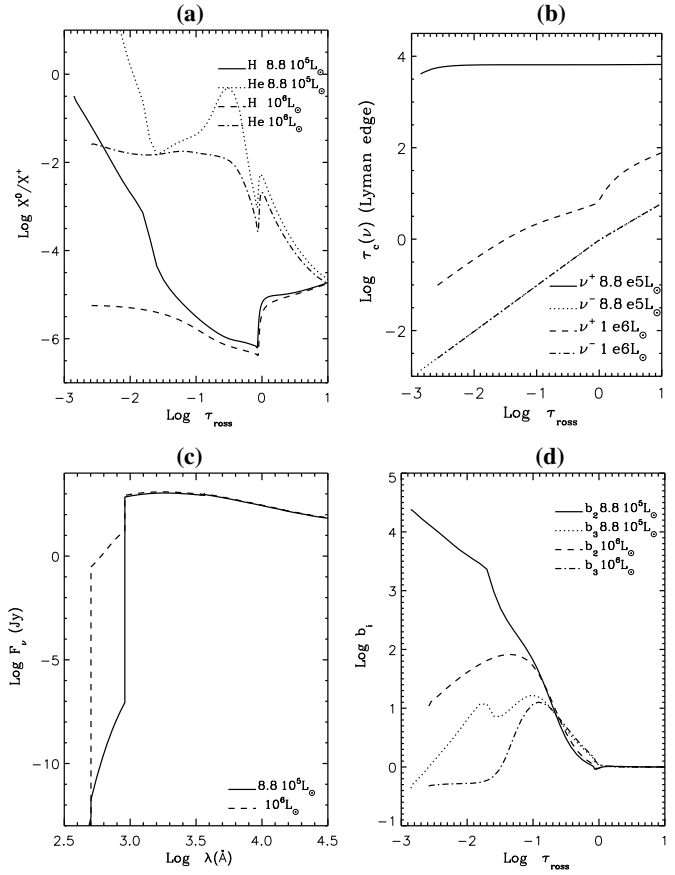

Fig. 1a–d. Comparison between the "ionized" and "recombined" models discussed in the text. **a** Run of the H I/H II and He I/He II ratio. Notice the large differences in both the H and He ionization structures. **b** Effects on the continuum opacity at the Lyman edge. Unlike the ionized model, the recombined model is optically thick in the Lyman continuum throughout the stellar wind. **c** Energy distributions showing the large reduction in flux shortward of the Lyman limit. Both models emit relatively little flux shortward of the He I edge at 584Å. **d** Behavior of the departure coefficients contributing to Hα. The enhanced population of level 2 in the recombined models gives rise to stronger absorption on Hα, in agreement with observation.

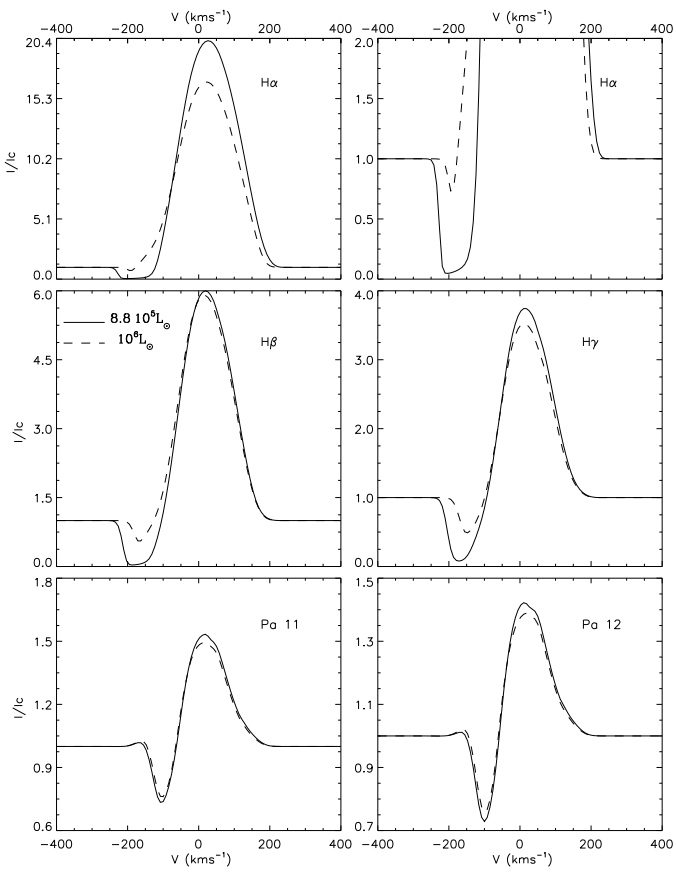

Fig. 2. Effects of changes in the wind ionization structure in the H profiles. The absorption components of the stronger Balmer lines are very sensitive to a switch in the wind ionization structure, while the profiles of the weaker Paschen lines are insensitive.

The factors determining the ionization structure, with specific reference to a recombined model, are discussed in Sect. 4.1.

The rapid change in the H ionization structure has dramatic effects on the energy distribution below the Lyman edge (see Fig. 1a–dc and discussion below) and is also reflected in the shape of the hydrogen profiles. If H recombines out in the wind, the population of the ground-state is tremendously increased. This leads to a dramatic increase of the opacity in the resonance lines (Lyman series), and in the optical depth of the Lyman continuum, which becomes optically thick throughout the entire wind (Fig. 1a–db). Consequently a large fraction of the Lyman continuum ionizing photons are removed (Fig. 1a–dc).

The strong P Cygni absorption of the Balmer lines can be reproduced only in the recombined model for reasons related to the increased opacity in the resonance lines. As a result of the increase in the optical depth in Lα, the second level of H is kept overpopulated in the wind, and acts as a metastable level so that the opacity of the Balmer lines is significantly enhanced.

This is illustrated in Fig. 1a–dd where we display the departure coefficients of the H n=2 and n=3 levels for the "ionized" and "recombined" models. As the reduced ionization of H in the "recombined" model prevents the n=2 departure from decaying for $\log \tau_{\rm R} < -1$, as in the "ionized" case, we expect the effects of recombination to be of greatest importance for those Balmer lines formed in the outermost layers (e.g., Hα and Hβ) of the wind. Closer to the star the departure coefficients behave similarly, and thus weaker lines should be similar in both the "ionized" and "recombined" models. The above is illustrated in Fig. 2 where computed recombined and ionized Hα, Hβ, Hγ, P_{11} and P_{12} profiles are shown for both the recombined and ionized models.

The influence of the ionization structure provides an explanation of why Kuan & Huhi (1975) required a decelerating velocity flow to match the absorption lines of P Cygni. They used the velocity law to maintain a high optical depth in the Balmer lines; this is done via the influence of the Lyman continuum and the Lyman lines in the "recombined" model

Although the changes in the He ionization structure are even more dramatic than for H, the *optical* He I lines remain basically unaffected. This is easy to understand as follows. First, the He emission lines are formed inside the radius at which He becomes neutral, even in the recombined model. Second, we note that the He I ground state bound-free opacity and resonance lines were already optically thick for the "ionized" model so that increasing the optical depth has little effect on the He I optical lines, for which the run of departure coefficients remains essentially unaltered.

Although the optical He I lines are insensitive to sudden changes in the He ionization structure ($\Delta \log L_* \leq 0.05$) we stress that these lines do react to normal changes in luminosity (i.e., 50%) within a "recombined" or "ionized" domain, and hence they provide a major constraint on the effective temperature of the star (Sect. 4.1).

The sensitivity of the ionization structure has important implications for variability observations. For example, when the wind is ionized, an increase in $\dot{M}$ (e.g., by shell ejection) may cause H and He to recombine. If recombination does take place it will dramatically reduce the emergent flux, particularly in the sub-millimeter and radio range (which originate in the outer wind). The P Cygni absorption may also undergo dramatic changes.

In the recombined model a slight reduction in mass loss may cause dramatic changes in the P Cygni absorption profiles. Mass loss changes in any direction will alter the ionization structure, and thus affect sub-millimeter and radio fluxes. Variations in ionization structure provide a simple explanation for the variability of P Cygni's radio fluxes found by van den Oord et al. (1985).

Changes in the wind ionization structure may explain some of the variability observed in stars like AG Car (Crowther 1994) where the stronger Balmer lines have been observed to switch between P Cygni (at maximum brightness in the visual) and pure emission (at minimum) shapes.

Using the nature of the observed Balmer lines together with the observed radio variability we conclude that the ionization structure of P Cygni resembles the "recombined" model shown in Fig. 1a–da. The "recombined" model keeps the Lyman lines optically thick and hence accounts for the absorption dips on the Balmer lines (particularly Hα), while the "ionized" model fails to reproduce the observed profiles. In addition, the short time scale of the observed radio variability is more easily explained in the recombined model (see Sect. 6).

4. Parameter space investigation

In the following sections we investigate how the structure of P Cygni's wind, the line profiles, and the continuous energy distribution vary with changes in L_*, $\dot{M}$, and the velocity parameters $h_{\rm eff}$ and β. We restrict ourselves primarily to "recombined models" – for the "ionized" case and the V_o velocity parameter the reader is referred to Najarro (1995).

Variations in R_* can be related to variations in $\dot{M}$ and $L_*(T_{\rm eff})$ via the scaling relations to be discussed in Sect. 5 and are therefore not considered.

4.1. Luminosity dependence

To investigate the influence of changes in the stellar luminosity ($T_{\rm eff}$) we compare three "recombined" models with

R_*=75 $R_\odot$ $\quad \dot{M}$= 5.75 $\times$ 10^{-5} $M_\odot$ yr^{-1}
V_∞=185 km s^{-1}, $\quad \beta$ = 2
$h_{\rm eff}$=7.5 $\times$ 10^{-3} R_* $\quad n_{\rm He}/n_{\rm H}$=0.8

as common parameters, and

L_*=7.25$\times 10^5$ $L_\odot$ ($T_{\rm eff}$=19.4 kK),
L_*=6.25$\times 10^5$ $L_\odot$ ($T_{\rm eff}$=18.7 kK),
L_*= 5.5$\times 10^5$ $L_\odot$ ($T_{\rm eff}$=18.1 kK)

for the luminosities.

We chose only a moderate maximum difference in L_* between the models ($\sim$35%) as we do not wish the atmospheric structures to depart significantly from that characterizing P Cygni, and as we show below, line profiles are sensitive to relatively small changes in L_*.

In Figs. 3a and Fig. 3b the behavior of the H and He ionization structure with radius and luminosity is shown. The large change in the H ionization ratio at $\log \tau_{\rm R} \approx 0$, in all models, is related to the huge decrease in the opacity of the resonance lines due to the (coupled) behavior of the velocity field and density.

For values of $\log \tau_{\rm R} \approx 0.5$ the intense radiation field in the hydrogen resonance lines, formed in the inner photosphere, has a radiation temperature higher than the local electron temperature. It begins to depopulate the ground state through pumping to the upper levels (as shown in Fig. 3d where the sum of the resonance lines' net rates is displayed).

As soon as the density drop (increase in velocity) occurs, induced Doppler shifts allow the resonance lines to absorb even more continuum photons (Najarro et al. 1996, Gabler et al. 1989). This enhances the depopulation of the ground state, and maintains the increased H ionization down to lower $\tau_{\rm R}$ values than is the case in a static atmosphere. The depopulation mechanism eventually ceases, either because the Doppler "support" is exhausted (i.e., flow has reached its terminal velocity) or because the radiation field in the resonance lines becomes diluted and ineffective for pumping. When this occurs the sum over the net rates changes sign ($\log \tau_{\rm R} \approx -0.4$ (Fig. 3d) and an overpopulation of the ground state results (Fig. 3a). As discussed in detail by Hillier (1987) a similar mechanism controls the He^+/He^{++} ionization ratio in WN stars.

In addition to the resonance lines, the intense Lyman continuum also contributes to depopulating the ground state. The importance of the Lyman continuum is enhanced by the density drop, and by the depopulation caused by the resonance lines. Consequently the ionizing photons have less ground-state population to traverse. This effect is related to the classical non-LTE dip in the departure coefficient of the ground state (Mihalas 1978).

The behavior of the Lyman opacity is shown in Fig. 3c where the velocity field and the continuum opacity times radius (so

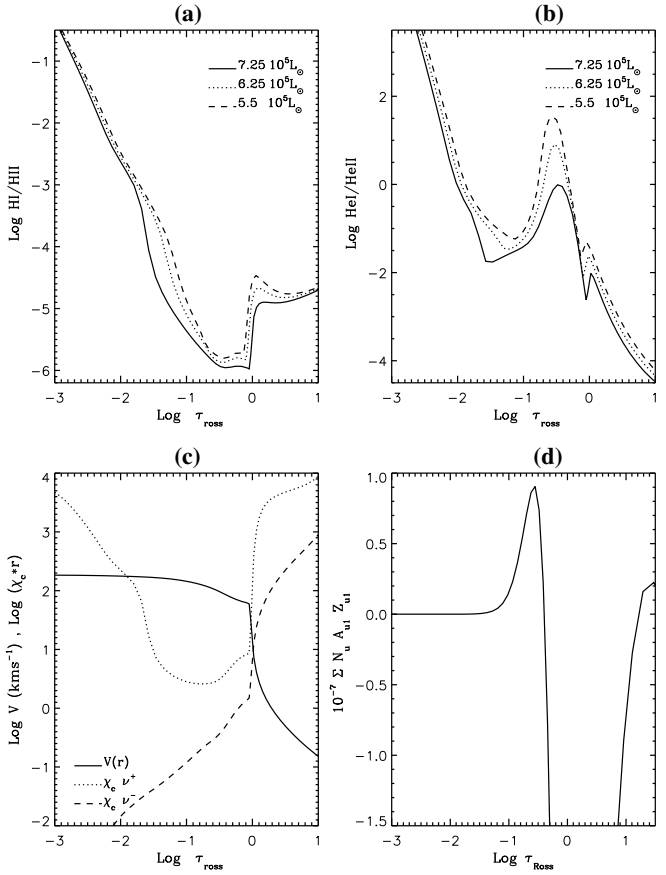

Fig. 3a–d. Illustration of various quantities for the "recombined" models as a function of L_*. Run of the **a** H I/H II and **b** He I/He II ratios. Notice that He becomes predominantly neutral around $\tau_R = -0.5$ which influences the strength of the He I lines. **c** Velocity field and continuum opacity shortwards and longwards the Lyman edge for the model with $L_*=7.25\times10^5 L_\odot$. Continuum opacity is multiplied by radius and hence dimensionless, so that $\int \chi r \, \mathrm{dlog}\, r$ gives the optical depth. **d** Net contribution of all Hydrogen resonance lines (in units of 10^7) to the ground state population as a function of optical depth for the "recombined" model with $L_*=7.25\times10^5 L_\odot$. A negative value denotes depopulation of the ground state through pumping to the upper levels, while a positive value denotes a net cascade to the ground state.

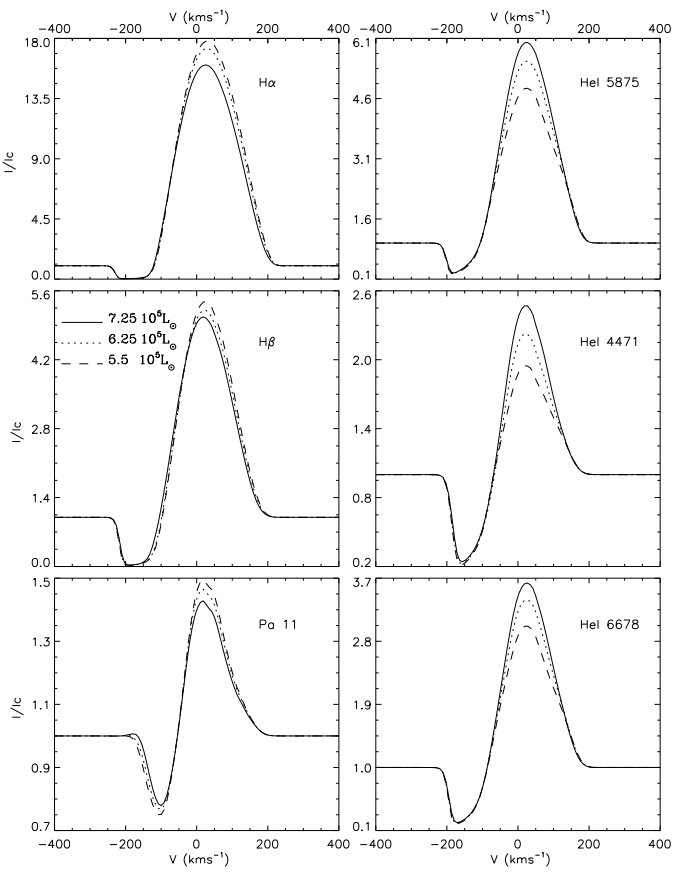

Fig. 4. Effects of changes in the stellar luminosity on H and He I profiles. A decrease in the luminosity slightly enhances the EW of the H lines but strongly reduces the emission components in the He I optical and near-IR lines which form in the region where the maximum in He I/He II occurs (around $\log \tau_R \approx -1.$ in Fig. 3b)

that the integral of this value over d log r gives the optical depth increment) shortwards and longwards of the Lyman edge are displayed as a function of optical depth for the model with $L_*=7.25\times10^5 L_\odot$. While the drop in the opacity longwards of the edge at $\log \tau_R \approx 0$ closely follows the jump in the density structure, as it is essentially dominated by electron scattering ($\sim n_e$), the decrease of the continuum opacity shortwards of the edge [denoted by $\chi_c(\nu^+)$] which is dominated by the ground-state population is considerably larger.

As long as the continuum opacity is not too large, the strong radiation field at the Lyman jump (remember that the energy distribution of the star peaks close to ∼1000Å) constitutes the main source of ionization. At $\log \tau_R \approx -1.6$ the ground level becomes so overpopulated (and therefore its bound-free opacity so large) that the Lyman continuum comes into detailed balance. This results in a considerable increase in the gradient of the ionization structure (Fig. 3a) and enhances the H I/H II ratio enormously. From this point outwards it is the second level which determines the ionization balance of H.

Though it appears to be rather complex, the run of the ionization structure of He (Fig. 3b) is relatively easy to understand. The bound-free opacity for the He I ground state is very large. Even at the density drop at $\log \tau_R \approx 0$ it exceeds the hydrogen value by a factor of ∼500, which results in only a small jump in the ionization degree (see Fig. 3b) that correspondingly decreases with decreasing luminosity (higher opacity). Further, since the resonance lines are in detailed balance throughout the atmosphere, they cannot depopulate the ground state. Thus, as soon as the density drop has been passed the He I bound-free opacity for the ground state is increased (up to 5 dex over the Lyman one) and the He I continuum also comes into detailed balance. The statistical equilibrium equation for the ground-state of He I is then determined by collisional excitations and de-excitations to the n=2 levels, which means that the ionization structure has to be coupled to the local electron temperature.

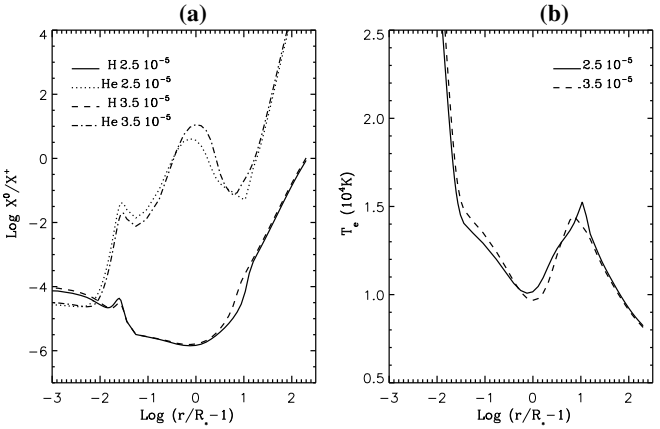

Fig. 5. a Run of the H I/H II and He I/He II ionization structure as a function of stellar radius for the "recombined" models with $\dot{M}$=2.5×10^{-5}M$_\odot$ yr^{-1} and $\dot{M}$=3.5×10^{-5}M$_\odot$ yr^{-1}. **b** Temperature distribution.

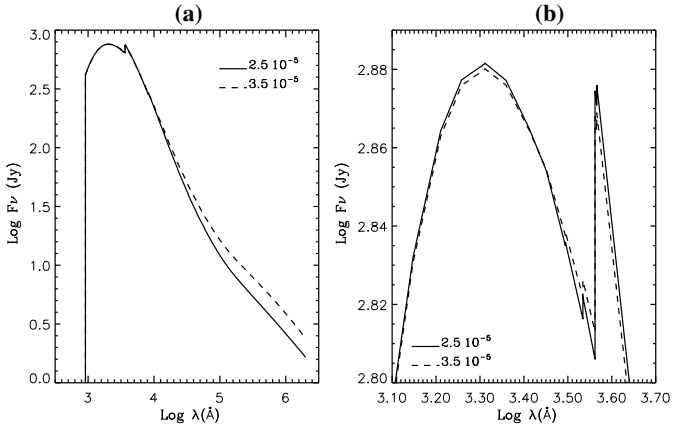

Fig. 6a and b. Run of the emergent energy distribution for the "recombined" models with $\dot{M}$=2.5×10^{-5}M$_\odot$ yr^{-1} and $\dot{M}$=3.5×10^{-5}M$_\odot$ yr^{-1}. **a** EUV to far-IR range, **b** range between Lyman and Balmer edges. The enhanced free-free excess of the higher mass-loss rate model is clearly evident longward of 1μm(log λ(Å) = 4).

The variation in line profiles with stellar luminosity is illustrated in Fig. 4. Lowering L$_*$ slightly enhances both the absorption and emission components in the H lines. The enhancement in emission (as measured by I/I$_c$) is primarily due to a reduction in the continuum flux.

The changes in the He I profiles are more dramatic, and are of opposite sense to those of the H lines. This can be simply understood by utilizing Fig. 3b. The reduced luminosity has decreased the ionization of He in the region the He I lines are formed. The relative variations in the strength of the He I lines is then primarily related to where the lines form in relation to the maximum in the He I/He II ratio.

An important conclusion from this work is that the emission components of the He I lines will reach their maximum for those values of L$_*$ where the switch from "ionized" to "recombined" structure is about to occur.

4.2. Mass-loss rate $\dot{M}$

Variations in mass-loss rate scale the global density structure of the atmosphere, and hence might be expected to influence all line profiles. To perform the investigation we consider two "recombined" models with

R$_*$=75 R$_\odot$	n$_{He}$/n$_H$=0.25
L$_*$=6×10^5 L$_\odot$	(T$_{eff}$=18.5 kK)
V$_\infty$=200 km s^{-1}	β = 1
h$_{eff}$=5 × 10^{-3} R$_*$	

as common parameters, and $\dot{M}$=2.5 × 10^{-5} M$_\odot$ yr^{-1} and $\dot{M}$=3.5 × 10^{-5} M$_\odot$ yr^{-1} for the mass-loss rates.

Because both models are "recombined," relatively small variations are seen in the ionization structures of H and He (Fig. 5a), and in the temperature distribution (Fig. 5b).

The behavior of continuum energy distribution is shown in Fig. 6. Changes in the UV are relatively small, while the higher mass-loss rate leads, as expected, to a higher free-free excess at longer wavelengths ($\lambda > 1\,\mu$m). Extensive discussions on the IR energy distribution are given in general terms by Panagia & Felli (1975) and Lamers & Waters (1984), and with specific reference to P Cygni by Najarro (1995).

Changes in the H profiles with $\dot{M}$ are illustrated in Fig. 7, while those for He I are shown in Fig. 8. Again we see that the H and He I lines show different sensitivities. The emission components of the hydrogen lines have strengthened with an increase in $\dot{M}$, while the absorption components of the higher Paschen lines have moved to higher velocities. No such shift is seen in lines such as Hα and Hβ which show saturated absorption components up to V$_\infty$.

The absorption components of the He I lines behave in a similar way (Fig. 8) to those of H, although some of them like He I 7281 Å clearly show the effects of the ionization structure. Surprisingly the emission components remain essentially constant. Normally we would expect the emission component to increase with an increase in mass-loss rate. This effect does not occur because of the competing effect of changes in the He I ionization.

4.3. Velocity field shape: β

For this investigation we consider four "recombined" models with

R$_*$=75 R$_\odot$	n$_{He}$/n$_H$=0.25
L$_*$= 6 × 10^5 L$_\odot$	(T$_{eff}$=18.5 kK)
$\dot{M}$=2.5 × 10^{-5} M$_\odot$ yr^{-1}	V$_\infty$=200 km s^{-1}
h$_{eff}$=5 × 10^{-3} R$_*$	

as common parameters, and β=1,2,4 and 6. Changes in β will primarily affect the density and velocity in the wind (e.g., Eq. 1).

The effects of changes in β on the ionization structure and temperature distribution for the "recombined" models are shown in Fig. 9. Significant changes in the ionization structure and temperature structure are seen to occur.

The high density of the β=4 model produces a curious extension effect. For the β=1 model, the continuum shortwards

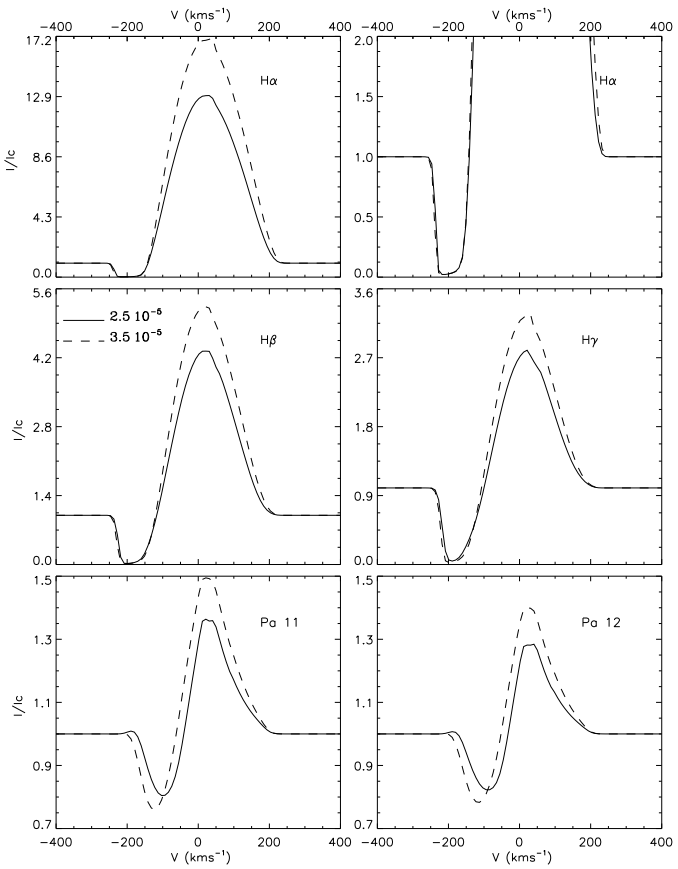

Fig. 7. Effects of changes in $\dot{M}$ on the H profiles. An increase in $\dot{M}$ significantly enhances the emission components and shifts the absorption dips to higher velocities.

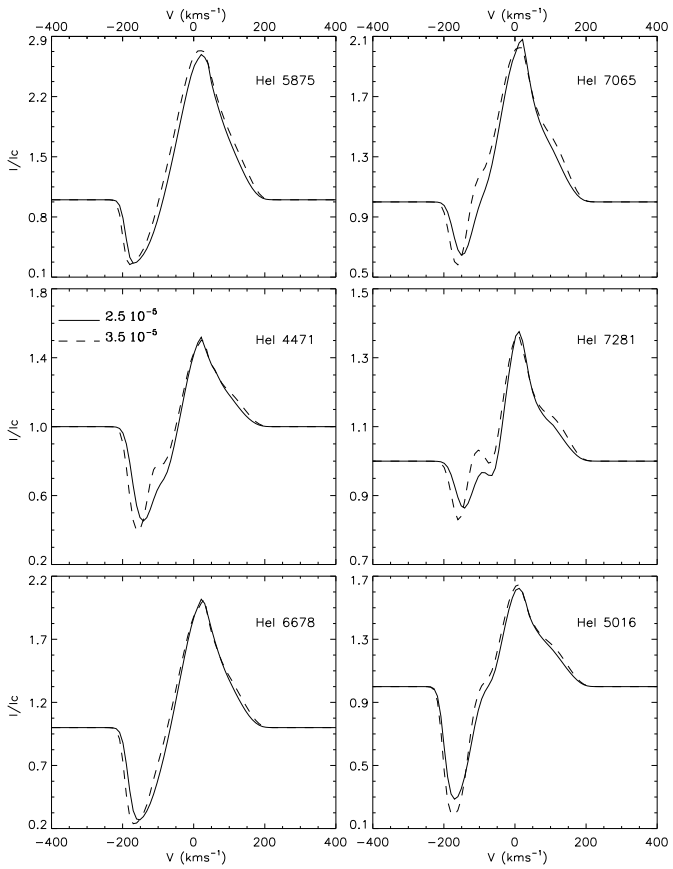

Fig. 8. Effects of changes in $\dot{M}$ on the He profiles. An increase in $\dot{M}$ enhances and shifts the absorption dips to higher velocities while the emission components show only minor changes. The peculiar double absorption dip on the He I 7281 line is due to the bump in the He ionization struction discussed earlier.

and longwards of the Balmer edge are both formed in the exponential-like density region, and hence the Balmer jump is in absorption. For the β=4 model, however, the higher density shifts the formation of the Balmer continuum to the region where the "plateau" in the velocity field occurs, while the continuum longwards of the edge is still formed in the high density "quasi-hydrostatic" region. This leads to a significantly higher effective emitting radius for the Balmer continuum and results in the Balmer jump being in emission (Fig. 10). The above effect depends critically on the assumed parameters, particularly on the choice of V_o.

For the H profiles an increase in β leads to an enhancement of the emission peaks at line center, the displacement of the absorption components to the red, and a smaller width of the lines. Of concern is the appearance of an emission component at larger negative velocities which is not only present in the high Paschen series, but which also starts to appear for the Balmer lines. The H line profiles provide an important β diagnostic.

The behavior of the He I profiles (Fig. 12) looks rather complex, but the shapes of the profiles are essentially related to the bump in the He ionization structure, which becomes quite extreme in the line formation regions for the high β models as shown in Fig. 11. The behavior of the absorption component in the He I 5016Å line is also interesting. The minimum is displaced to redder values but absorption still occurs until $-V_\infty$. The reason for the latter is that the lower level of this transition, $2s\,^1S$, is metastable.

4.4. Effective scale height $h_{\rm eff}$

P Cygni represents an interesting intermediate case between O stars and W-R stars. In O stars the effective scale height (i.e., effective gravity) is crucial for analyzing the spectrum and can be determined observationally, while in W-R stars the scale-height is unimportant and has little influence on the observed spectrum.

To investigate effects of changes in $h_{\rm eff}$ we have chosen two "recombined" models with

R_*=75 $R_\odot$	n_{He}/n_H=0.4
L_*=7.25×10^5 $L_\odot$	($T_{\rm eff}$=19.4 kK)
$\dot{M}$=3.4 × 10^{-5} $M_\odot$ yr^{-1}	V_∞=185 km s^{-1}
β=4	

as common parameters and $h_{\rm eff}$=7.5 × 10^{-3} R_* $h_{\rm eff}$=3 × 10^{-2} R_* respectively. The effective scale-height values cor-

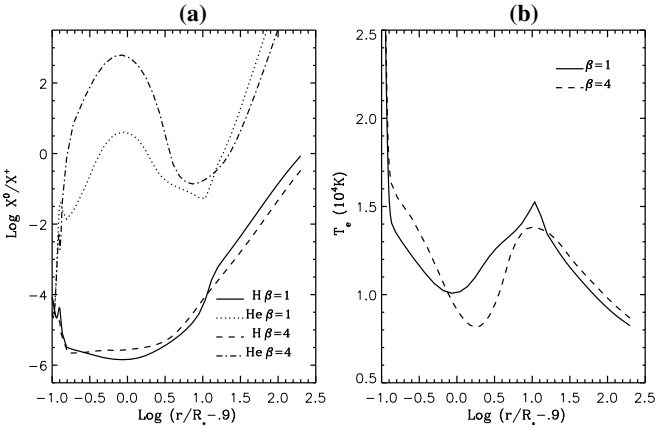

Fig. 9. a Run of the H I/H II and He I/He II ionization structure as a function of stellar radius for the "recombined" models with β=1 and β=4. **b** Temperature distribution.

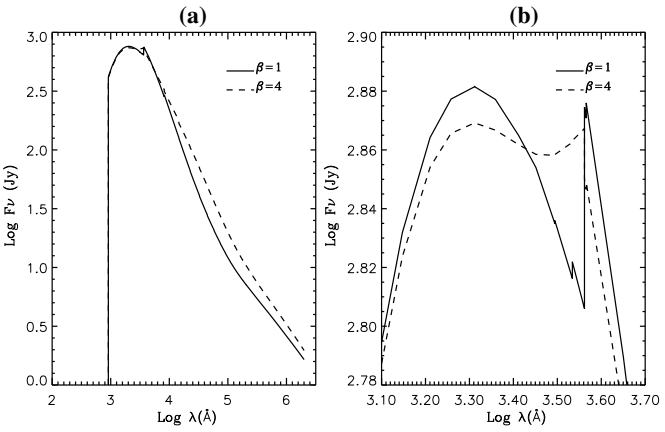

Fig. 10a and b. Run of the emergent energy distribution for the "recombined" models with β=1 and β=4. Notice that the Balmer jump is in emission in the β = 4 model and that because of the higher wind density the β = 4 model has a larger IR excess. **a** EUV to far-IR range. **b** Range between Lyman and Balmer edges.

respond roughly to effective gravities of log g_{eff}≈1.7 and log g_{eff}≈1.1 and Γ_e≈0.5 and Γ_e≈0.8.

We display the run of the velocity and density together with $\sigma = d\log v/d\log r - 1$ as a function of $\log(r/R_* - 1)$ in Fig. 14. From Fig. 14a we see that both models have the same density in the outer regions, while in the inner regions the model with the larger h_{eff} leads to a lower velocity and hence a higher density. It is also important to note the much smaller jump in σ for the high h_{eff} model which is related to the nature of the analytical velocity field we have adopted in which V_o is reached at smaller R values for the lower h_{eff} model (steeper hydrostatic structure). We should expect variations in σ to affect processes involving the resonance lines as well as line profiles formed in these regions.

The first important effect of increasing h_{eff} is the outward shift of the photospheric radius. For the high h_{eff} value τ_R=2/3 is reached at $\log(r/R_* - 1) \approx -0.7$ ($1.2R_*$) while for the low

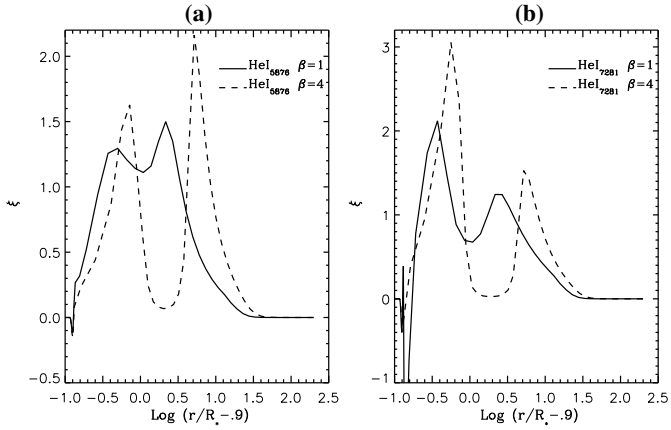

Fig. 11a and b. Effects of β on the contribution to He I line formation regions in the "recombined" models. **a** He I 5876Å. **b** He I 7281Å. The bump in the He I/He II distribution for the high β model splits the formation region of the lines. ξ(r) correspond to the contribution of each depth to the EW of the line (Hillier 1989), sothat EW=$\int_{R_*}^{\infty} \xi(r) d\log r$.

h_{eff} values this occurs at $\log(r/R_* - 1) \approx -1.3$ ($1.05R_*$). This means that although in principle we have two models with the same L_* and core radius, we are actually seeing two different "photospheric" radii and hence two different T_{eff} values are obtained. Thus, the extended model has $R_{2/3}$≈$90R_\odot$ and T_{eff}≈1.775 kK while the low h_{eff} model gives $R_{2/3}$≈$83R_\odot$ and T_{eff}≈1.897 kK. As a result we obtain two different energy distributions peaking at different wavelengths (Fig. 15a).

Significant changes in the H and He ionization structures are also seen (Fig. 15b), even in the wind. These changes primarily reflect the importance of the rapid density drop in determining the H ionization structure (compare Fig. 15b with Fig. 14) and the subsequent formation of the Lyman continuum.

The line formation regions of both the H and He I lines remain basically unaltered. Therefore observed changes in the strengths of the lines should simply reflect differences in the run of the ionization structure. From Fig. 15b we note that, on average, the amount of He II contributing to the He I lines in the wind is similar for both models. Furthermore, since both curves run roughly parallel to each other, no significant effects should be expected in the He I profiles. This result is fully confirmed by our calculations. Only the He I 5016Å line reflects minor effects of changes in h_{eff} with a slightly higher peak at line center for the high h_{eff} model.

From Fig. 15b we see that changes in h_{eff} induce major changes in the H ionization structure around $\log(r/R_* - 1) \approx -1$ and, therefore will affect those lines which form in this inner region. This is the case of the emission components of the high Paschen series as shown in Fig. 16. The effects on the Balmer lines displayed in Fig. 16 is caused by the change in the H ionization ratio over the entire wind region.

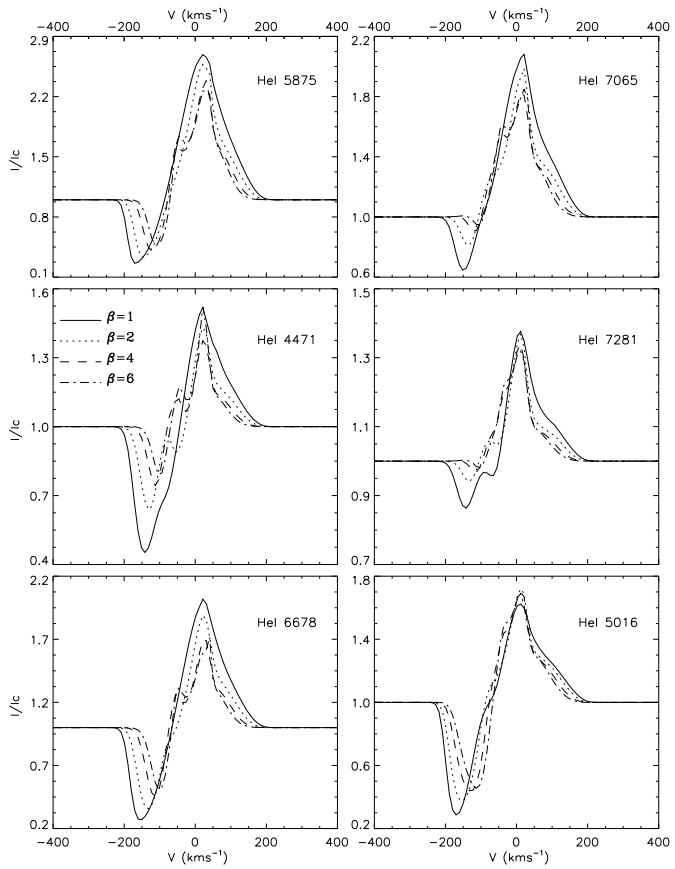

Fig. 12. Effects of changes in β on the He profiles for the "recombined" models. An increase in β significantly shifts the absorption dips to lower velocities.

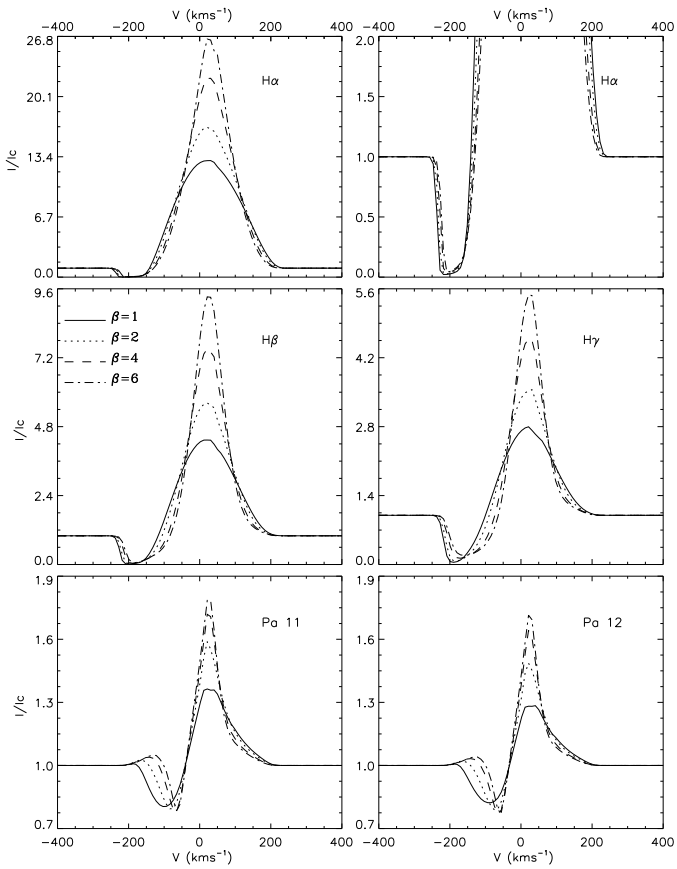

Fig. 13. Effects of changes in β on the H profiles for the "recombined" models. An increase in β significantly enhances the emission components and shifts the absorption dips to lower velocities, making the line widths narrower. The H lines provide an important β diagnostic.

5. Model ambiguity: the "wind density parameter"

Schmutz (1988) pointed out that the equivalent widths of the H and He wind emission lines in W-R stars are determined by two basic parameters: the stellar temperature and the so called "wind density parameter" $R_T \equiv \dot{M}/(V_\infty R_*^{3/2})$. The latter is not a physical density, but rather a numerical result such that similar "wind densities" will result in similar line equivalent widths, and in continuum energy distributions with the same shape. Similar results concerning the flux distribution had already been obtained by Panagia & Felli (1975) and Lamers & Waters (1984) from IR- and radio-continuum investigations, while the $\dot{M}/R_*^{3/2}$ relation in Hα was pointed out by Leitherer (1988).

The above may be understood as follows. First, both the continuum and line fluxes will scale as $S R(\tau = 1)^2$ where S is the source function. This is obviously true for the continuum formed in a plane-parallel atmosphere, but is also true when extension effects are important, and is also true for the lines (e.g., Hillier et al. 1983). The proportionality factor will differ in the two cases but for the parameters of interest they can be assumed to be constant.

Second, we assume that the level populations are primarily determined by recombinations, and thus proportional to the product of the electron (N_e) and ion (N_i) densities. Thus, if the velocity law is of the form $v(\bar{r}) = V_\infty\,(1 - b/\bar{r})^\beta$, where b is a constant and $\bar{r}$ is in units of R_*, the opacity χ will be set by the product $N_e N_i$ and thus,

$$\chi \propto \frac{\dot{M}^2}{V_\infty{}^2 R_*{}^3}\ \frac{g(\bar{r})}{\bar{r}^4\,(1 - b/\bar{r})^{2\,\beta}}\ \frac{1}{R_*}$$

where $g(\bar{r})$ accounts for the behavior of the ionization structure and the $1/R_*$ term has been factorized as it will cancel when computing the optical depth.

From these assumptions it follows that at fixed $T_{\rm eff}$ the parameter determining the line and continuum fluxes is $\dot{M}/(V_\infty R_*^{1.5})$. The choice of fixed $T_{\rm eff}$ preserves, to first order, the source function S and the ionization structure $g(r)$. Thus models with different density parameters and the same $T_{\rm eff}$ should have a similar continuum shape, and further the lines should have similar equivalent widths. This result has been confirmed by Schmutz et al. (1989) and Crowther (1994) who showed that different stellar parameter combinations for which (R_T, T_*) was maintained led only to small differences (rarely greater than 15-20%) in the resulting line EWs.

To investigate the "wind density parameter" for P Cygni-like models we initially chose three models with R_*=60, 75

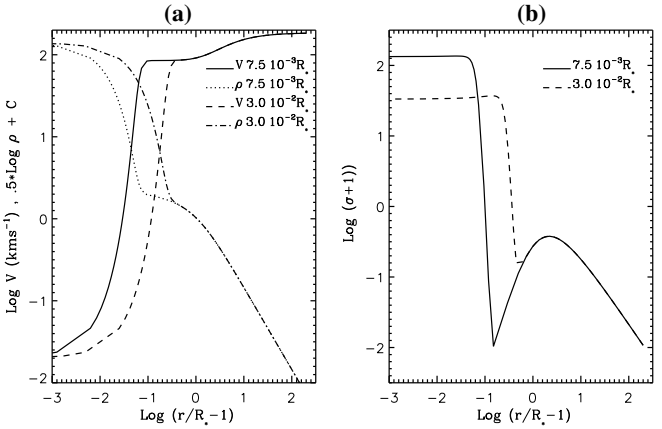

Fig. 14a and b. Effects of h_{eff} on the velocity field and density structure **a** and σ **b**

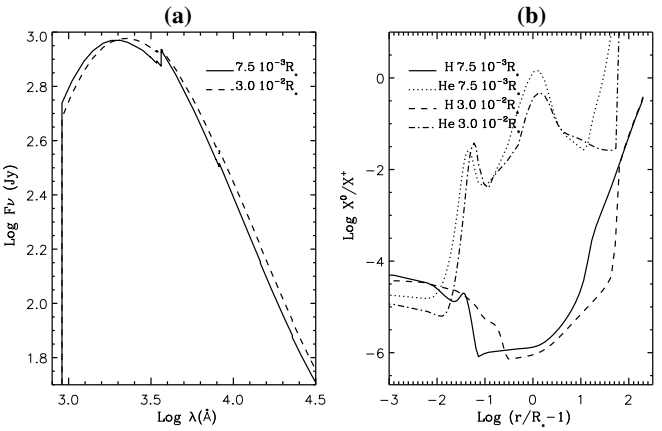

Fig. 15a and b. Effects of h_{eff} on the energy distribution and ionization structure for "recombined" models. **a** Run of the emergent energy distribution for models with h_{eff}=7.5×10^{-3}R$_*$ and h_{eff}=3×10^{-2}R$_*$ between the Lyman jump and 3μm. **b** H and He ionization structure

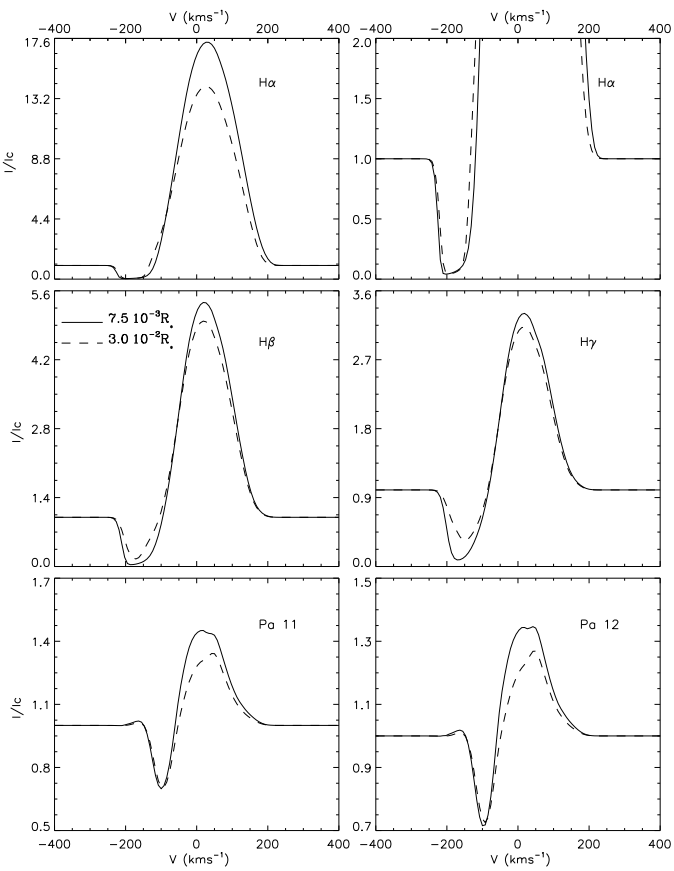

Fig. 16. Effects of changes of h_{eff} on the H profiles for the "recombined" models. An increase in h_{eff} significantly weakens both the emission and absorption components. (see discussion in text)

and 90 R$_\odot$ respectively and scaled $\dot{M}$ and L$_*$ correspondingly to keep R$_T$ and T$_*$ fixed. The resulting flux distributions F$_\nu$ are almost identical, with a small ($\sim$4%) difference between the 60 and 90 R$_*$ models in the 3–20μm region. The excellent agreement is somewhat surprising given the simplicity of our assumptions. In particular we might expect differences as some processes (e.g., electron scattering) do not scale as the density squared.

The similarity in temperature and ionization structure for the two models with R$_*$=60R$_\odot$ and R$_*$=90R$_\odot$ is shown in Fig. 17. While the changes are small, they are sufficient to produce *non-negligible* changes in the line profiles.

Our results indicate that homologous R$_T$ transformations in which R$_*$ is increased require a slightly lower T$_*$ in order to keep the ionization degree of the species and temperature as a function of $\bar{\tau}$ unchanged, and therefore to obtain identical line profiles. To quantify the required transformations we performed a parameter space investigation for 6 different stellar radii (R$_*$= 30, 40, 60, 75, 90 and 130 R$_*$).

The reference was a "recombined" model with the following parameters:

R$_*$=75 R$_\odot$	L$_*$= 7.25 × 10^5 L$_\odot$
$\dot{M}$=3.35 × 10^{-5} M$_\odot$ yr^{-1}	V$_\infty$=185 km s^{-1}
β=4	h_{eff}= 7.5 × 10^{-3} R$_*$
n$_{He}$/n$_H$=0.4	

For each R$_*$ we transformed $\dot{M}$ and L$_*$ with respect to the model with R$_*$=75 R$_\odot$(R$_{*75}$) as ($\dot{M}/\dot{M}_{75}$)$\propto$(R$_*$/R$_{*75}$)^a and (L$_*$/L$_{*75}$)$\propto$(R$_*$/R$_{*75}$)^b, and each (a,b) pair was fine-tuned until we obtained roughly the same ionization and temperature structures as in the R$_*$=75 R$_\odot$ case. Despite the large range of R$_*$ considered, a tight relationship was obtained, which as expected did not differ considerably from the above discussed R$_T$,T$_*$ homologous transformations. We obtained the following coefficients:

$$\left(\frac{\dot{M}_2}{\dot{M}_1}\right) = \left(\frac{R_{*2}}{R_{*1}}\right)^{1.43\pm0.03}$$
$$\left(\frac{L_{*2}}{L_{*1}}\right) = \left(\frac{R_{*2}}{R_{*1}}\right)^{1.71\pm0.03}$$
$$\left(\frac{T_{*2}}{T_{*1}}\right) = \left(\frac{R_{*2}}{R_{*1}}\right)^{-0.072\pm0.007} \quad (2)$$

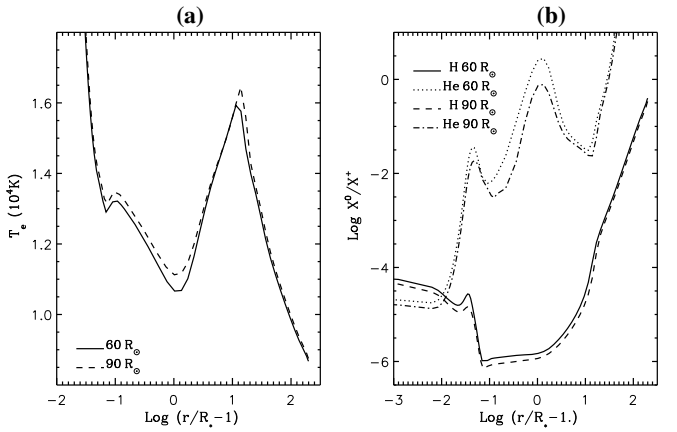

Fig. 17a and b. Effects of homologous R_T transformations on the temperature distribution and ionization structure with increasing R_*. **a** Temperature distribution. **b** H and He ionization structure.

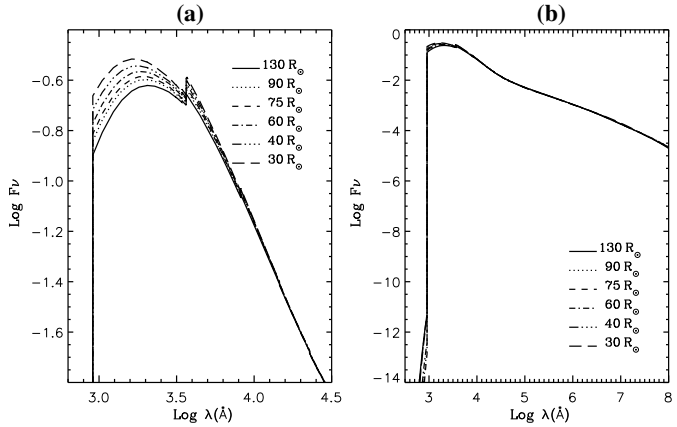

Fig. 18a and b. Effects of homologous R_T transformations on the flux distribution and ionization structure with varying R_*. Curves have been shifted by a common factor to better compare their shapes. **a** UV, optical and near-IR. **b** Full λ range.

To test the validity of these results within the parameter space of interest we repeated the procedure for a set of "ionized" models. The coefficients were identical to those given in Eq. 2 within half the standard deviations.

While the optical line profiles obtained with this parameterization are very similar, the new parameterization differs slightly from the usual R_T–T_* and thus non-negligible differences appear in the shape of the flux distributions of the objects. This is shown in Fig. 18a,b where we have displayed the continuum energy distributions for the "recombined" series, and where each curve has been scaled to overlap in the IR. From Fig. 18a,b we note that although the shapes of the curves are identical for λ>8000Å, they differ moderately in the UV and the optical. Therefore, continuum observations in the latter regions could, at least in principle, provide a useful tool to separately obtain the value of the stellar radius R_* and hence the stellar distance.

Unfortunately the advantage of using UV and optical observations for determining R_* and hence the distance is overcome by the presence of line blocking in the UV and reddening in both the UV and optical regions. Reddening effects can fully simulate the fluxes obtained with different R_* values and hence we conclude, especially when allowances are made for both observational and model errors, that the absolute value for R_* and hence the stellar distance cannot be obtained from a spectroscopic analysis alone.

6. A model for P Cygni

6.1. Current best model.

To model P Cygni in detail, nitrogen (N II - N III) was included with an abundance of $n_N/n_{He}=2\times10^{-3}$ (increased to account for mixing with CNO cycled matter). Improved model atoms consisting of 15 H, 51 He I ($n\leq11$), 5 He II, 43 N II and 11 N III levels were adopted. Detailed modeling using the Sobolev approximation and then the co-moving frame method to fine tune the model parameters led to the following stellar values:

R_*=75 $R_\odot$	
L_*=5.6×10^5 $L_\odot$	([5.0 to 7.0]×10^5 $L_\odot$)
$T_{\rm eff}$=1.82 kK,	(1.77 to 1.92 kK)
n_{He}/n_H=0.3	(0.25 to 0.55)
$\dot{M}$=3.0×10^{-5} $M_\odot$ yr^{-1}	([2.6 to 5.0]×10^{-5} $M_\odot$ yr^{-1})
V_∞= 185 km s^{-1}	(175 to 200 km s^{-1})
β=2.5	
V_o=30km s^{-1}	
$h_{\rm eff}$=2.2 × 10^{-2} R_* (log $g_{\rm eff}$=1.20)	

As noted in Sect. 5 the value for R_* was adopted since it cannot be deduced by a spectroscopic analysis. We chose R_*=75 $R_\odot$ for historical reasons as this value was derived by Lamers et al. (1983) from a study of the energy distribution of P Cygni together with an estimate for the distance to the object (d≈1.8 kpc) from cluster membership considerations. We shall discuss the adequacy of this value in Sects. 6.2 and 6.4. The "best" values of L_* ($T_{\rm eff}$) and $\dot{M}$ for other choices of R_* can be found by using the scaling relations given by Eq. 2.

The model parameters of our best co-moving frame model differ minimally from those obtained with the Sobolev approximation. The only discrepancy arises in the $h_{\rm eff}$ value derived with the Sobolev approximation ($h_{\rm eff}=7.5\times10^{-3}$ R_*, log $g_{\rm eff}$=1.68). That the value of $h_{\rm eff}$ differs between the two models is not surprising – the Sobolev model is not expected to be valid in the inner regions where continuum absorptions are important, where the velocities are small, and where there are rapid changes in the source functions.

Because of the interplay between the various parameters it is difficult to gauge the errors in our determinations. Outside the range of parameters listed above the profile and continuum fits are noticeably worse. The errors on the individual parameters are NOT independent. To give some insight into the accuracy of the parameter determinations we note that the best fit model *without* N had $T_{\rm eff}$=1.92 kK and n_{He}/n_H=0.4. Further the best fit model also uses recent ISO observations as additional constraints. The ISO data between 2.5 and 10μm provide the more reliable diagnostics to constrain the velocity field. These observations necessitated the revision of β from 4 to 2.5 and V_o from

80 km s^{-1}to 30 km s^{-1}. These revisions actually led to much better fits of the the He I 4713 Åand 4120 Å lines. These errors ignore possible systematic effects (e.g., the neglect of blanketing in our models, and the possible influence of clumping) and the implications of wind variability in P Cygni. Of particular concern is the difficulty in constraining the velocity law accurately – other effects (e.g., ionization) can be used to compensate for velocity law changes. New ISO IR observations will provide an additional important constraint.

In order to test the adequacy of using a constant scale height in our models, we relaxed this approximation by letting h be a function of local electronic temperature, h=h$_{\rm eff}$ T(r)/T$_{\rm eff}$ (where h$_{\rm eff}$ is the value used for the models with constant scale height). Though the correct description of the problem can only be achieved by an accurate solution of the hydrostatic equation in the inner parts of the photosphere (work in progress), the above assumption, when introduced into our velocity field, provides a more physical density stratification than the use of a constant scale height. We carried out a parameter study and obtained a higher h$_{\rm eff}$ factor (by $\sim$50%) needed to avoid the density structure becoming too steep in the transition region. The other model parameters coincide with those obtained for the CMF model with constant h$_{\rm eff}$ except L$_*$ increased by 4%. Both CMF models with and without constant h$_{\rm eff}$ produced identical line profiles.

6.2. Comparison with observations

Line profiles were computed for our best CMF model. To account for effects of non-coherent electron scattering in the profiles, we first evaluated the electron scattering emissivity by means of an iterative CMF calculation and then interpolated it onto the observer's frame where more accurate profiles can be computed. A turbulent velocity of V$_{\rm tur}$=15 km s^{-1} was used in both schemes and the resulting profiles were then "corrected" for rotation assuming a v sin i in the range of 30 to 45 km s^{-1}. We discarded the rather high value of 65km s^{-1} obtained by Uesugi & Fukada (1982, see also Vardya 1985) as the H computed profiles, when broadened by the latter, showed poor agreement with the observations. Finally, the resulting profiles were shifted to correct for the radial velocity. For the latter we obtained V$_{\rm rad}$=−29 km s^{-1} in agreement with the value obtained by Stahl et al. (1993). Line profiles were computed for the main observed optical H and He I lines and are discussed below. The following theoretical profiles were adjusted using v sin i=35 km s^{-1} and V$_{\rm rad}$=−29 km s^{-1}.

6.2.1. Hydrogen lines

Fig. 19a shows the fit of our computed Hα profile to the mean observed profile. Because of the high value at the emission peak, the region below I/I$_c$=2 has been expanded in Fig. 19b to show the absorption component and the electron scattering wings. We find excellent agreement between the theoretical and observed profiles. The absorption component of Hα is also well reproduced, while we obtain slightly stronger electron scattering wings than observed. While the use of an angle averaged redistribution function will slightly overestimate the electron scattering wings the presence of inhomogeneities in the wind can probably account for the above discrepancy (Hillier 1991).

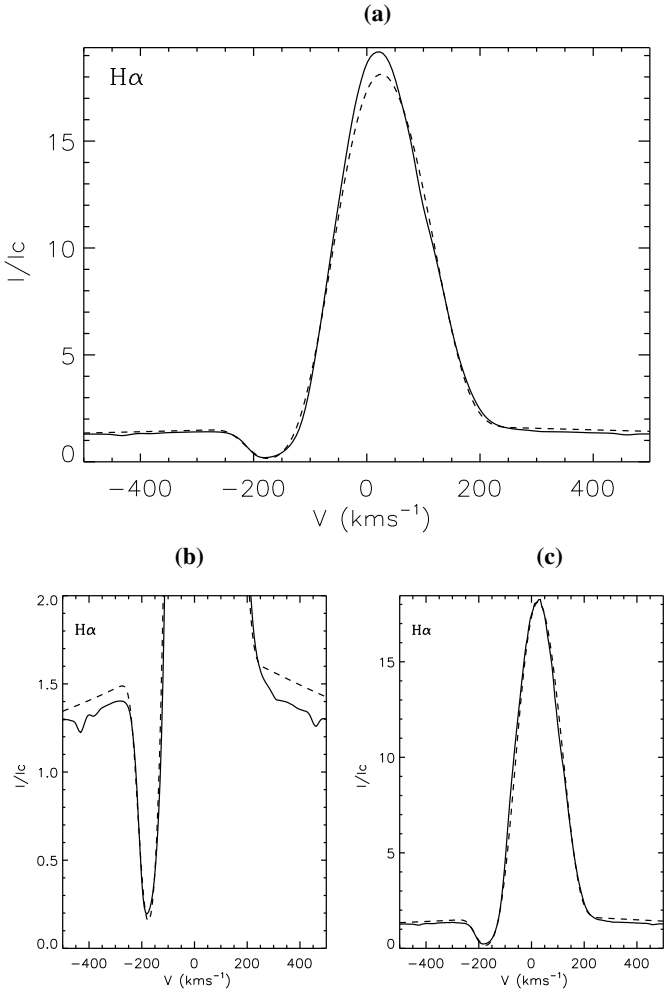

Fig. 19a–c. Comparison of observed (solid) and computed (dashed) Hα profiles. **a** Averaged observed Hα profile. **b** Expansion of region below I/I$_c$=2 highlighting the electron scattering wings and the absorption profile. As the model wings are slightly larger than those observed clumping may be important in P Cygni's wind. **c** Comparison of our computed Hα profile (dashed) with a single observed profile (solid).

It is important to stress that we are fitting an averaged profile and that the Hα line in P Cygni is highly variable (Stahl et al. 1994 quote variations in the emission peak intensity which range from 13 to 24 over the continuum during their $\sim$1000 days monitoring campaign). To illustrate the above we compare the Hα theoretical profile with a single snap-shot of Hα obtained by Stahl et al. in Fig. 19c. The agreement shown in this plot is superb.

Fig. 20 shows the excellent agreement between the observed and computed Hβ and Hγ profiles. As for Hα we also compare our theoretical profiles with a single snap-shot of the lines. The fit to Hβ is "self-explanatory" and needs no further comment. For Hγ our model produces a slightly higher emission peak and

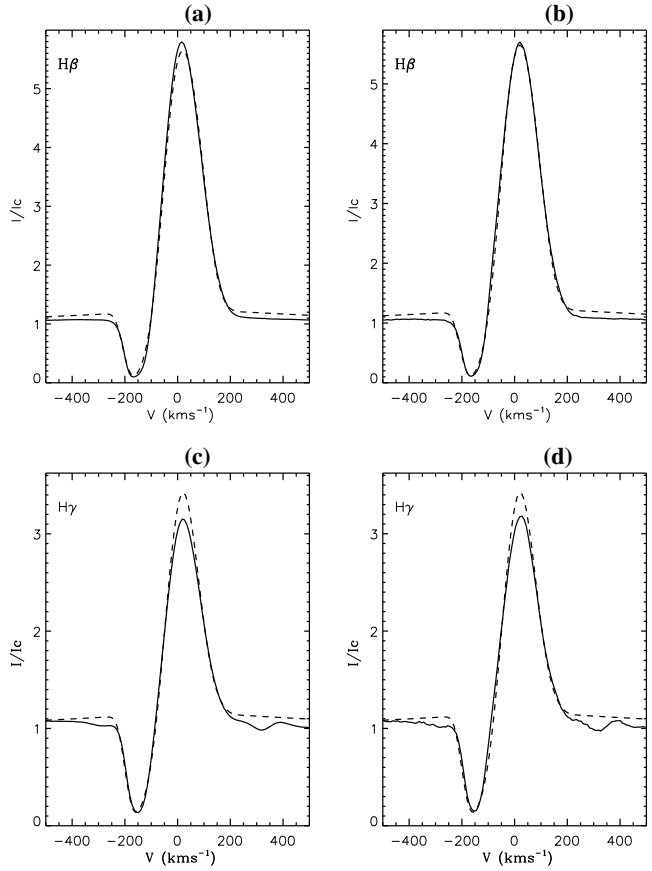

Fig. 20a–d. Comparison of observed (solid) and computed (dashed) Hβ and Hγ profiles. **a** Averaged observed Hβ profile. **b** Single observed Hβ profile. **c** Averaged observed Hγ profile. **d** Single observed Hγ profile.

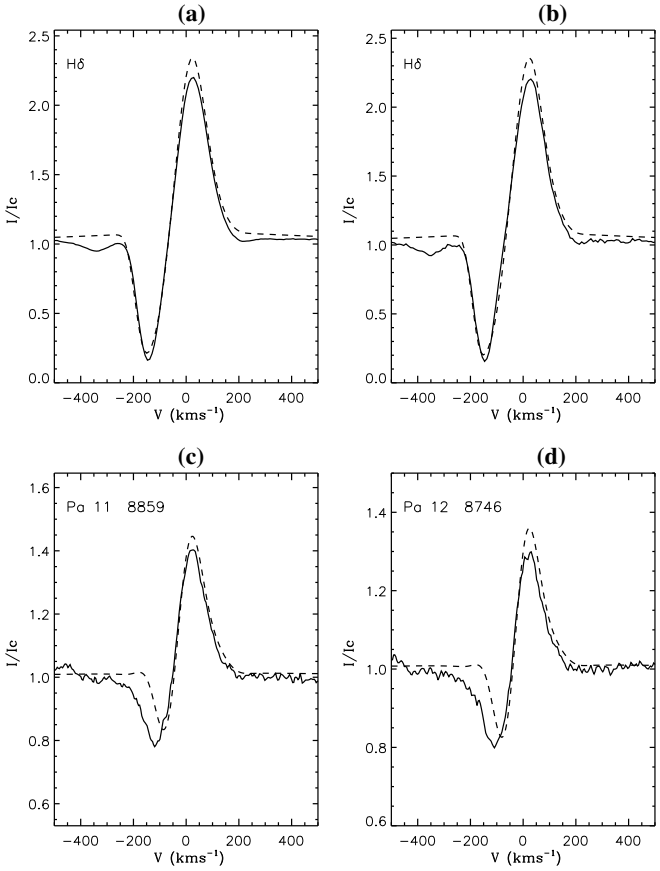

Fig. 21a–d. Comparison of observed (solid) and computed (dashed) Hδ and Paschen 11 and 12 profiles. **a** Averaged observed Hδ profile. **b** Single observed Hδ profile. **c** Averaged observed P11 profile. **d** Averaged observed P12 profile.

weaker absorption dip. This trend is clearly augmented in the Hδ line and in the higher Paschen lines as shown in Fig. 21. For the P11 and P12 lines this effect is extreme as the wind emission in our models fills in the absorption component at higher velocities and produces a small emission bump at v≈ -175 kms. The absorption components in the high Paschen series are very sensitive to the transition region between photosphere and wind (V_o).

6.2.2. Helium lines

In Figs. 22, 23 and 24 we compare 12 representative He I lines in the observed region with our corresponding theoretical profiles. The observed single snap-shots of the lines do not differ considerably from the averaged spectra chosen for the comparison. Fig. 22 shows the good agreement obtained for the triplet 2^3P–3^3D 5876Å (the strongest He I line in the optical) and 2^3P–4^3D 4471Å transitions, and the singlet 2^1P–3^1S 7281Å and 2^1S–3^1P 5016Å lines. Excellent agreement with the observations is also obtained for the singlet 2^1P–n^{1}D and the triplet 2^3P–n^{3}S transitions as shown in Figs. 23 and 24. Interestingly, the triplet 3^3P–10^3L 8582Å transition shows the same kind of discrepancy with the observations as that found for the high Paschen series.

While excellent agreement is found for all relevant singlet transitions and the majority of the triplet lines in He I, our models underestimate the emission components of the high 2^3P–n^{3}S series, for reasons, we believe, to be related to the neglect of line blanketing.

6.2.3. Continuum energy distribution

Fig. 25 shows the fit of the emergent continuum energy distribution of our best model to the observations. UV data were obtained with the S2/68 Ultraviolet Sky Survey Telescope and the International Ultraviolet Explorer satellite (Lamers et al. 1983). Visual observations are from Johnson & Mitchell (1975), near-IR observations from Abbott et al. (1984) and IRAS observations from Waters & Wesselius (1986). Submillimeter and radio data have been taken from the compilation by Wendker (1987), Altenhoff et al. (1994, 1.3mm), Becker & White (1985, 2cm) and White & Becker (1982, 6cm). The correction for interstellar extinction was derived using the model continuua and the reddening law of Rieke & Lebofsky (1985). We obtain a value

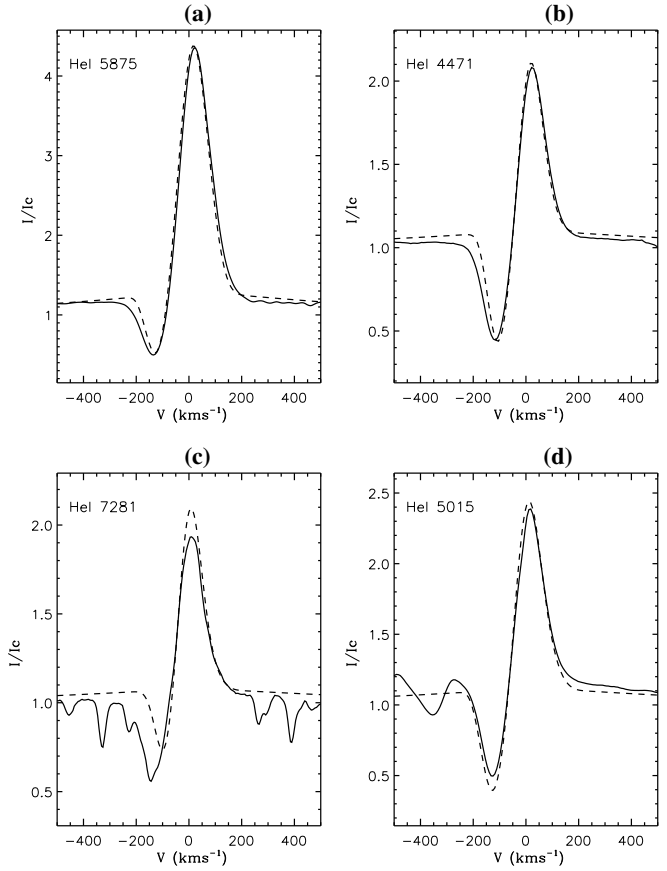

Fig. 22a–d. Comparison of observed (solid) and computed (dashed) He I profiles. **a–b** Triplet 2^3P–3^3D 5876Å and 2^3P–4^3D 4471Å lines. **c–d** Singlet 2^1P–3^1S 7281Å and 2^1S–3^1P 5016Å lines.

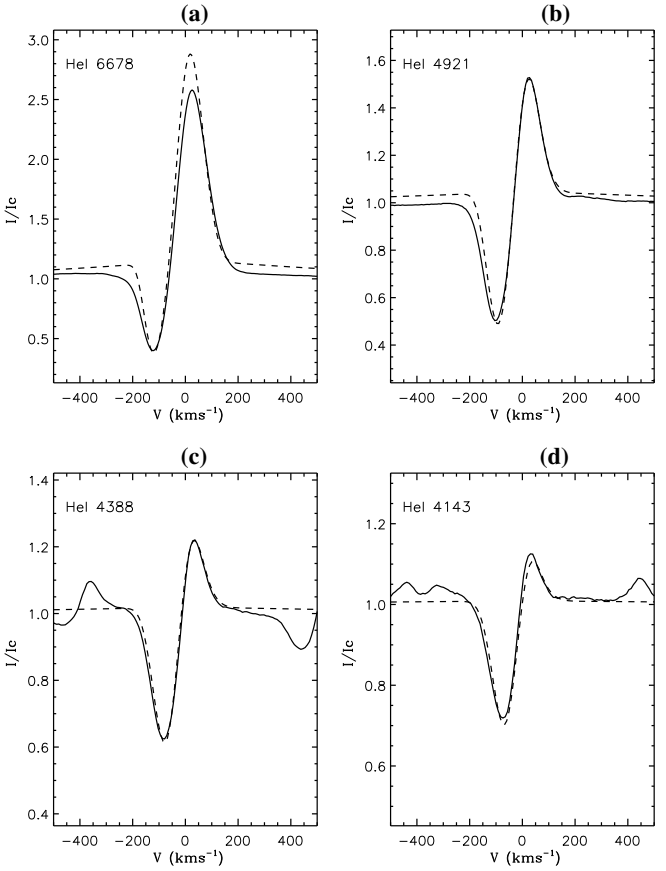

Fig. 23a–d. Comparison of observed (solid) and computed (dashed) He I profiles. **a–d** Singlet 2^1P–n^{1}D (n=3 to 6) line series. Excellent agreement with the observations is found.

of E(B−V)=0.51±0.02 which is slightly slower but consistent with that derived by Lamers et al. (1983) from the Lα interstellar absorption line (E(B−V)=0.57), and from spectral type and UV energy distribution comparisons with other supergiants (E(B−V)=0.63).

Fig. 25a shows that our models reproduce, within the observational errors, the energy distribution of P Cygni for the wavelength range 2500Å$\leq\lambda\leq$ 60μm reasonably well. For $\lambda\leq$2500Å, however, the observed flux is strongly blocked, and therefore cannot be reproduced by our models. Line blanketing is especially strong in the region around 2000Å, where the Fe III complex ($\lambda\lambda$ 1887-2098) causes a broad absorption dip (Pauldrach et al. 1989). From Fig. 25a it becomes evident that line blanketing effects will have to be incorporated into the model as they play a major role in the UV energy distribution of P Cygni and therefore will also significantly affect the H resonance lines.

Another important characteristic of the energy distribution of P Cygni (displayed in Fig. 25b) is the enhanced variability on time scales of the order of months (Abbott et al. 1981) observed in the submillimeter and radio region compared with the optical. This effect was discussed by van den Oord et al. (1985) who concluded that the time scale of these variations could not be interpreted in terms of density variations but was due to changes of ionization in the wind. Our model results confirm this interpretation, as the wind region where the H I/H II ratio becomes greater than one coincides with the submillimeter and radio continuum forming region. Thus, tiny changes in luminosity or mass-loss rate will shift the location in the wind where H I=H II and therefore will considerably change the effective emitting volume contributing to the emission in this wavelength range. The flux distribution for shorter wavelengths (IR and optical) on the other hand will remain basically unaffected. Moreover, if recombination takes place, we should also expect the spectral index (α) for the flux distribution $F_\nu\propto\nu^\alpha$ to depart from the canonical value for a fully ionized wind ($\alpha\approx$0.6, Wright & Barlow 1975).

As shown by Hartmann & Cassinelli (1977; see also Schmid-Burgk 1982), a stellar wind with an ion density distribution $\propto 1/r^n$ and a temperature structure $T(r)\propto 1/r^m$ has a spectral index $\alpha\sim$(4n−0.6m−6.2)/(2n−1.35m−1). From the recombined models, in which the ionization in the outer wind is maintained by photoionizations from the n=2 state of H, the ion and electron density both vary as $r^{-3.5}$. As the temperature distribution remains fairly flat ($T(r)\propto 1/r^{0.1}$) we obtain a value of $\alpha\approx$1.3 in those regions where H I/H II$\gg$1. Therefore we should

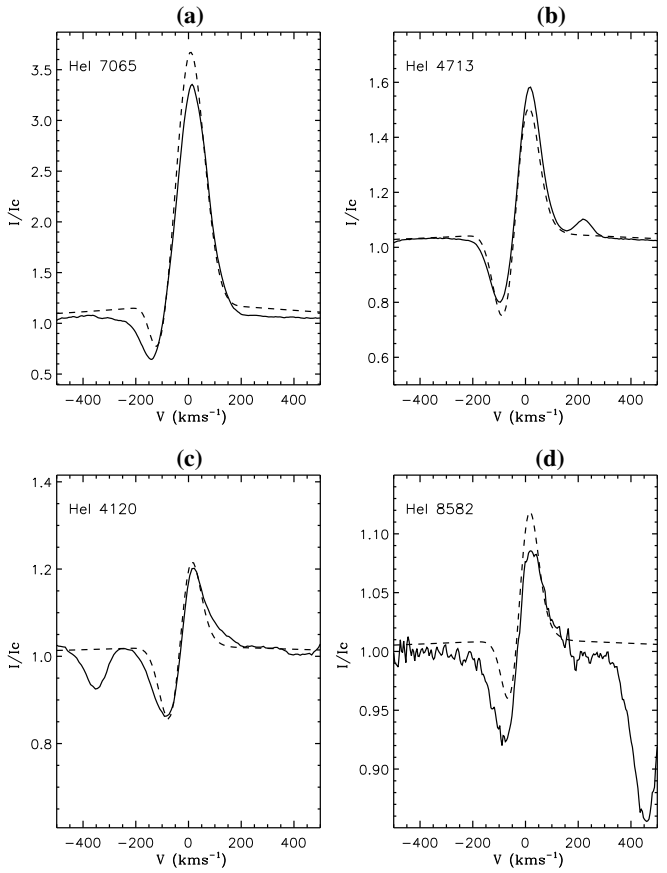

Fig. 24a–d. Comparison of observed (solid) and computed (dashed) He I profiles. **a–c** Triplet 2^3P–n^{3}S (n=3 to 5) line series. **d** Triplet 3^3P–10^3L 8582Å transition.

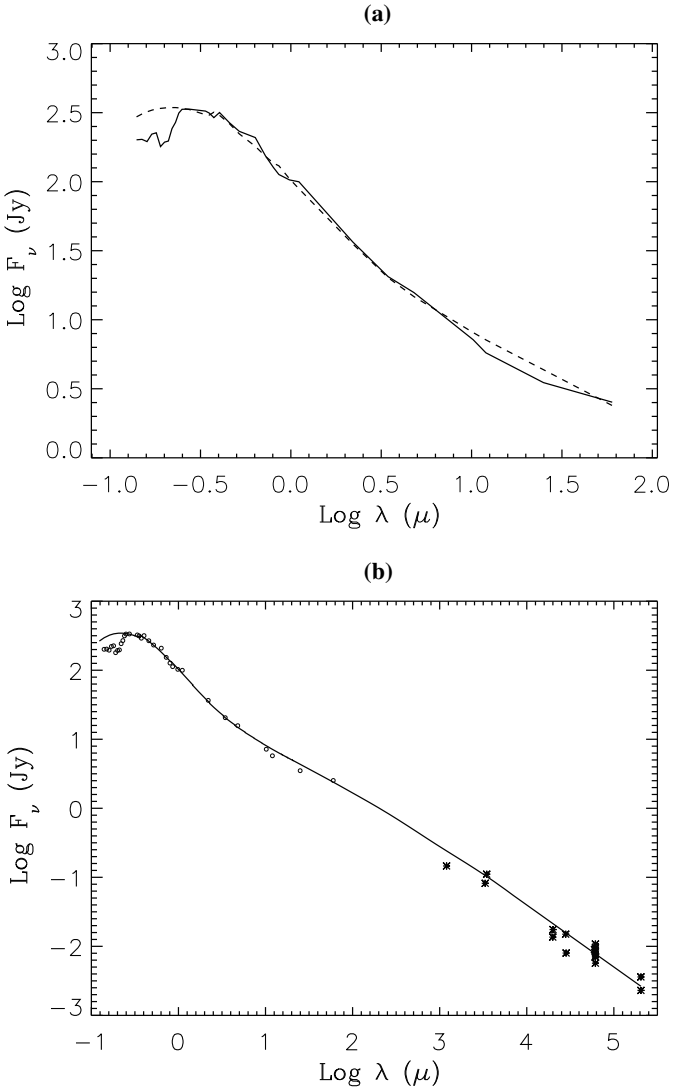

Fig. 25a and b. Comparison of observed (solid) and computed (dashed) continuum energy distributions. The derived distance and extinction coefficients are d=1.7kpc (for R_*=75$R_\odot$) and E(B-V)=0.51 respectively **a** UV, optical and IR spectrum. **b** Full UV to radio spectrum

expect the spectral index to change from 0.6 in those regions where H I/H II$\ll$1 to 1.3 far out in the wind where H I/H II$\gg$1.

In our model, as the submillimeter and radio continuum (1mm$<\lambda<$6cm) form in those regions where 0.1$<$H I/H II$<$5, the spectral index varies roughly between $\alpha\approx$0.8 at 1.3mm and $\alpha\approx$1.0 at 6cm (see Fig. 25b). If recombination did not occur in the wind ("ionized" models) the wind density required to reproduce the H and He I profiles would lead to a too strong excess at radio wavelengths.

We conclude that the "recombined" picture for the wind of P Cygni offers a plausible explanation for the observed radio variability and produces a continuum energy distribution consistent with observations from $\lambda>$2500Å to $\lambda\sim$20cm.

6.3. Distance

For our model with R_*=75$R_\odot$ and with E(B$-$V)=0.51 the implied distance is d=1.7$\pm$0.1 kpc. The latter value is in agreement with that proposed by Lamers et al. (1983) d=1.8$\pm$0.1 kpc based on cluster membership determinations, and the value of d=1.6 kpc derived by Beals (1951) from the velocity of the interstellar lines and a model for the differential galactic rotation.

Apart from cluster association measurements we may obtain an estimate for the stellar radius (and hence $\dot{M}$, L_* and distance) using the wind momentum luminosity relation (Kudritzki et al. 1995) and the scaling relations given in Eq. 2. This method yields $R_*\approx127R_*$, $L_*\approx1.75\times10^6L_\odot$, $\dot{M}\approx6.8\times10^{-5}M_\odot$ yr^{-1} and d$\approx$2.5 kpc. Unfortunately this estimate has a large error as the slope of the wind momentum luminosity relation and the scaling ratio of Eq. 2 are similar. Thus, values of R_* ranging between 50$R_\odot$ and 150$R_\odot$ lie within the standard deviation of this method.

6.4. Significance of P Cygni's model parameters

6.4.1. Hydrodynamics

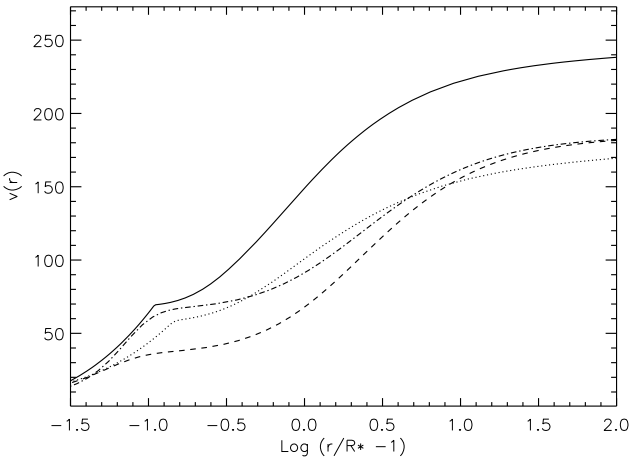

Fig. 26. Comparison of analytical and hydrodynamical velocity fields. The hydrodynamical results for low Γ and low $\dot{M}$ **(solid)** and high Γ and high $\dot{M}$ **(dotted)** show qualitatively good agreement with a model (dashed-dotted) with slightly higher V_o and same β than our best model (dashed).

To check the consistency of our derived velocity distribution we compare in Fig. 26 the run of velocity for our best model against that obtained from hydrodynamical calculations (Pauldrach; priv. comm.). Also shown is the velocity field for a model with slightly higher V_o (65 km s^{-1}) and the same β (2.5) value. The hydrodynamical models were calculated following the procedure of Pauldrach et al. (1989) but also included bound-free and free-free processes, and multi-line effects (Puls 1987). The latter was performed under the plausible assumption that line-overlap behaves qualitatively in the same way for the model parameters discussed here and those considered by Pauldrach et al. (1989).

The upper hydrodynamical curve in Fig. 26 was obtained for a low Γ value (Γ is the ratio of Thompson radiative acceleration to gravitational acceleration) for which the resulting Lyman continuum in the wind is optically thin and therefore a lower $\dot{M}$ and high V_∞ are obtained. The lower curve corresponds to a higher Γ value for which an optically thick continuum results and a high $\dot{M}$ (similar to that from our models) and low V_∞ are obtained. From Fig. 26 we see that our derived analytical velocity field shows similar qualitative behavior to the hydrodynamical models. Moreover, we note that only slight changes in V_o and β are required to obtain a velocity field resembling those models. Results of a quantitative investigation including hydrodynamical models will be presented in a follow-up paper.

6.4.2. Evolutionary status

An important result from our spectroscopic analysis of P Cygni is the enhanced helium abundance n_{He}/n_H=0.3 corresponding to a mass fraction Y_s of 0.63. P Cygni's helium abundance is moderately well constrained by the optical He I profiles and their ratios to the hydrogen lines. We find n_{He}/n_H=0.55 and n_{He}/n_H=0.25 as upper and lower limits respectively; the range in values is determined by the trade-off between He abundance and ionization. A similar value of He^+/H^+=0.5$\pm$0.1 was derived by Barlow (1990) and Deacon & Barlow (1990) who analysed H and He I near infrared recombination line fluxes.

Our value for the effective scale height $h_{eff} \approx 2.2 \times 10^{-2}\, R_*$ provides a rough estimate for the effective gravity ($\log g_{eff} \approx 1.2$) which gives $\log g \approx 2.0$ and $M \approx 18\, M_\odot$ if we crudely assume that the correction to the stellar gravity is basically determined by electron scattering processes.

The above results are consistent with those obtained by Pauldrach from radiation driven wind models presented in Langer et al. (1994). In that paper a step was made towards obtaining a consistent picture of P Cygni from evolutionary calculations, radiation driven wind theory and detailed spectroscopic analysis. Using the latest version of the OPAL opacities (Iglesias et al. 1992) and including the results of pulsational analysis of Kiriakidis et al. (1993) in a parametric way a new evolutionary scenario for very massive stars was proposed. This relates O stars, LBVs and W-R stars as follows: O $\rightarrow$ Of $\rightarrow$ H-rich WN $\rightarrow$ LBV $\rightarrow$ H-poor WN $\rightarrow$ H-free WN $\rightarrow$ WC $\rightarrow$ SN. A similar evolutionary scenario was derived by Crowther et al. 1995 from analysis of WN8 and Ofpe/WN stars.

Our results from the spectroscopic investigation, together with those from the radiation driven wind models and evolutionary calculations place P Cygni in the hydrogen shell burning phase of the evolutionary sequence of a 60 $M_\odot$ Zero Age Main Sequence (ZAMS) star. The star is found to be at the beginning of its LBV phase towards the red turnover in the H-R diagram in agreement with its observed visual brightening over the last centuries, which indicates a decrease of T_{eff} at a rate of 6$\pm$1% per century (Lamers & de Groot 1992, de Groot & Lamers 1992).

7. Summary

A detailed parameter space investigation, within the domain of interest, was performed to gain further understanding into the nature of P Cygni and its wind, and the origin of its unusual spectrum. Our analysis indicates that the optical and near infrared H and He I profiles are sensitive to changes in stellar luminosity, mass-loss rate, the shape of the velocity field and the effective scale height, allowing quantitative analyses to be performed.

The stellar parameters for P Cygni place it near a regime where small changes in these parameters (e.g. 5% in $\dot{M}$) may cause a dramatic change in the wind structure. In particular we find two classes of models – those in which H is ionized throughout the wind, and those in which both H and He recombine in the outer wind. This sensitivity is similar to the bi-stability mechanism of Pauldrach & Puls (1990) except we treat $\dot{M}$ as a free model parameter. Consequently there is no feedback between the ionization structure and $\dot{M}$.

From a detailed study of the H Balmer profiles (particularly Hα) we conclude that both He and H must recombine in the outer parts of the wind. Only a recombined wind is capable of producing the saturated P Cygni absorption on the Hα profile.

Further, only a recombined wind provides a mechanism to explain the rapid variations in radio continuum fluxes found by van den Oord et al. (1985).

As for W-R stars, it is not possible to determine the stellar radius using spectroscopic analyses. Models with different stellar parameters can produce spectra which are observationally identical. For the case of P Cygni we found transformation relations for R_*, $\dot{M}$ and L_* ($T_{\rm eff}$) which lead to a set of homologous models with very similar line profiles and continuum distribution shapes. These scaling relations are similar to those of Schmutz et al. (1989) who found that models with the same wind density parameter ($\dot{M}/V_\infty R_*^{1.5}$) and effective temperature produce similar W-R spectra.

The adequacy of the Sobolev approximation accounting for diffuse continuum processes outside the resonance zone was also discussed. While for the same model parameters the Sobolev and CMF methods may show differences in line profiles and continuum fluxes, the stellar parameters obtained for the best model will differ only slightly from those obtained using the CMF method. Therefore the faster Sobolev approximation provides reliable first estimates for the stellar parameters which can be fine-tuned by means of the CMF method.

Armed with the knowledge of line formation in the wind of P Cygni we performed a detailed spectroscopic investigation of P Cygni using the observational constraints given by observed mean averaged optical and near infrared H and He I spectra, and UV to radio photometric measurements available in the literature. The stellar parameters for our best model are:

R_*=75 $R_\odot$ $\dot{M}$=3.0 $\times$ 10^{-5} $M_\odot$ yr^{-1}
L_*=5.6$\times 10^5$ $L_\odot$ $T_{\rm eff}$=1.82 kK
n_{He}/n_H=0.3 V_∞= 185 km s^{-1},
β=2.5 $h_{\rm eff}$=2.2 $\times$ 10^{-2} R_* (log $g_{\rm eff}$=1.20)

Our computed line profiles and continuum fluxes are in excellent agreement with those observed.

The mass-loss rate for P Cygni is much higher than that for O stars, and is similar to that found for many W-R stars although the ratio of wind momentum to stellar momentum is still less than unity ($\dot{M}V_\infty/(L/c)$ = 0.48). Our derived mass-loss rate is in reasonable agreement with earlier determinations however we stress that the ionization structure of P Cygni's wind must be accounted for when determining mass-loss rates. Clumping may be important in the wind of P Cygni as the strength of the electron-scattering wings on Hα is slightly overestimated. On the other hand, reasonable agreement is obtained between the optically derived mass-loss rate and that obtained from the radio. Unfortunately radio variability hampers this comparison.

The derived H/He abundance ratio and stellar parameters indicates that P Cygni is highly evolved, and places the object on the hydrogen burning shell phase moving towards the red turnover in the H–R diagram. Our results show good agreement with those obtained from recent evolutionary calculations and radiation driven wind models.

Work is in progress to deduce an accurate N abundance and to include the effects of Fe blanketing. This should allow a more accurate H/He ratio to be computed, and will allow even tighter constraints to be placed on the evolutionary status of P Cygni. Additionally we are using ISO data to check the consistency of the model, and to determine whether ISO data can provide additional constraints on the structure of P Cygni's wind.

Acknowledgements. F. N. acknowledges a grant of the DARA under WE2- 50 OR 9413 6. The calculations have been carried out on the Cray YMP 4/32 of the Bayerische Akademie der Wissenschaften.

References

Abbott D.C., Bieging J.H., Churchwell E., 1981, ApJ, 250, 645
Abbott D.C., Telesco C.M., Wolf S.C., 1984, ApJ, 279, 225
Altenhoff W.J., Thum C., Wendker H.J., 1994, A&A, 281, 161
Barlow M.J., 1990, in: IAU Symp. 143, Wolf-Rayet Stars and Interrelations with Other Massive Stars in Galaxies, eds. K. A. van der Hucht and B. Hidayat, Reidel, Dordrecht, Holland p. 281
Barlow M.J., Cohen M., 1977, ApJ, 213, 737
Beals C.S., 1951, Publ. Dominion. Astrophys. Obs., IX, 1
Becker R.H., White R.L., 1985, in Radio Stars, ASSL 116, eds. R.M. Hjellming, D.M. Gibson, p. 139
Crowther P.A., 1994, PhD Thesis, University of London
Crowther P.A., Smith, L.J., Hillier D.J., Schmutz W., 1995, A&A, 293, 427
Deacon J.R., Barlow M.J., 1990, in: IAU Symp. 143, Wolf-Rayet Stars and Interrelations with Other Massive Stars in Galaxies, eds. K. A. van der Hucht and B. Hidayat, Reidel, Dordrecht, Holland p. 558
de Groot M., 1989, in: Physics of Luminous Blue Variables, eds. K. Davidson, A.F.J. Moffat, H.J.G.L.M. Lamers, Kluwer, Dordrecht, p. 257
de Groot M., Lamers H.J.G.L.M., 1992, Nature, 355, 422
Drew J.E., 1985, MNRAS, 217, 867
Gabler R., Kudritzki R.P., Pauldrach A.W.A., Puls J., 1989, A&A, 226, 162
Glatzel W., Kiriakidis M., 1993, MNRAS, 263, 375
Hartmann L., Cassinelli J.P., 1977, ApJ, 215, 155
Hillier D.J., Jones T.J., Hyland A.R., 1983, ApJ, 272, 221
Hillier D.J., 1987, ApJ Suppl., 63, 947
Hillier D.J., 1989, ApJ, 347, 392
Hillier D.J., 1990, A&A, 231, 116
Hillier D.J., 1991, A&A, 247, 455
Hillier D.J., 1996, ApJ, 271, 221
Iglesias C.A., Rogers F.J., Wilson B.G., 1992, ApJ, 397, 717
Johnson H.L., Mitchell R.I., 1975, Rev. Mex. de Astronomía y Astrofísica, 1, 299
Johnson D.R.H., Barlow M.J., Drew J.E., Brinks E., 1992, MNRAS, 255,261
Kuan P., Huhi L.V., 1975, ApJ, 199, 148
Kiriakidis M., Fricke K.J., Glatzel W., 1993, MNRAS, 264, 50
Kudritzki R.P., Lennon D.J., Puls,J. 1995, Proc. ESO Conference, "Science with the VLT", eds. J.R. Walsh, I.J. Danziger, p 246
Lamers H.J.G.L.M., Waters L.B.F.M., 1984, A&A, 136, 37
Lamers H.J.G.L.M., de Groot M., 1992, A&A, 257, 153
Lamers H.J.G.L.M., 1986, in Luminous Stars and Associations in Galaxies, IAU Symp. No. 116, eds. C.W.H. de Loore, A.J. Willis and P. Laskerides, Reidel, Dordrecht, p. 157
Lamers H.J.G.L.M., de Groot M., Cassatella A., 1983, A&A, 128, 299
Langer N., Hamann W.-R., Lennon M., et al. 1994, A&A, 290, 819
Leitherer C., 1988, ApJ, 326, 356
Mihalas D., 1978, Stellar Atmospheres, 2nd Edition, Freeman, San Francisco
Najarro F., 1995, PhD Thesis, University of Munich

Najarro F., Kudritzki R.P., Cassinelli J.P., Stahl O., Hillier D.J., 1996, A&A, 306, 892
Panagia N., Felli M., 1975, A&A, 39, 1
Pauldrach A., Puls J., 1990, A&A, 237, 409
Pauldrach A., Puls J., Kudritzki R.P., 1989, in: Physics of Luminous Blue Variables, eds. K. Davidson, A.F.J. Moffat, H.J.G.L.M. Lamers, Kluwer, Dordrecht, p. 261
Puls J., 1987, A&A, 184, 227
Rieke G.H., Lebofsky M.J., 1985, ApJ, 288, 618
Schmid-Burgk J., 1982, A&A, 108, 169
Schmutz W., 1988, in IAU Colloquium 108, Atmospheric Diagnostics of Stellar Evolution: Chemical Peculiarity, Mass Loss and Explosion, ed. K. Nomoto (Lecture Notes in Physics, Vol. 305), Springer, Berlin, p. 133
Schmutz W., Hamann W-R., Wessolowski U., 1989, A&A, 210, 236
Schmutz W., Leitherer C., Hubeny I., Vogel M., Hamann W-R., Wessolowski U., 1991, ApJ, 372, 664
Stahl O., Mandel H., Wolf B., et al., 1993, A&AS, 99, 167
Stahl O., Wolf B., Gäng Th., et al., 1994, A&AS, 107, 1
Stothers R., Chin C.-W, 1994, ApJ, 426, L43
Taylor M., Nordsieck K. H., Schulte-Ladbeck R. E., Bjorkman K.S., 1991, AJ, 102, 1197
Uesugi A., Fukuda I. 1982, in Revised Catalog of Stellar Rotational Velocities, Kyoto University, Kyoto
van Blerkom D., 1978, ApJ, 213, 737
van den Oord G.H.J., Waters L.B.F.M., Lamers H.J.G.L.M. et al., 1985, in Radio Stars, Astrophysics and Science Library, Vol. 116, eds. R.M. Hjellming, D.M. Gibson, Reidel, Dordrecht, p. 111
Vardya M.S., 1985, ApJ, 299, 255
Waters L.B.F.M., Wesselius P.R., 1986, A&A, 155, 104
Wendker H.J., 1987, A&AS, 69,87
White R.L., Becker R.H., 1982, ApJ, 262, 657
Wright A.E., Barlow M.J., 1975, MNRAS, 170, 41

This article was processed by the author using Springer-Verlag LaTeX A&A style file *L-AA* version 3.